

GEONEUTRINO OSCILLATIONS APPROACH TO
DISCRIMINATE DISTRIBUTIONS OF HEAT
PRODUCING ELEMENTS IN THE EARTH'S
MANTLE

DANIEL FELIPE FORERO SÁNCHEZ
201415069

ADVISOR: JUAN CARLOS SANABRIA PhD.

This dissertation is submitted for the degree of
PHYSICIST



Physics Department
Faculty of Science
Universidad de Los Andes
Bogotá, Colombia
April 20, 2018

Dedicated to my little niece, Ana María,
without whom this thesis would have been
finished much, much earlier.

Abstract

Neutrinos are still an intriguing matter in physics due to their odd properties, nevertheless there is a rising field on Neutrino Geoscience using their unique properties to study the Earth. This project shows the results of the simulations done in order to calculate the expected geoneutrino (electron antineutrinos from natural beta decay) signal from different mantle distributions of Heat Producing Elements and Bulk Silicate Earth models. The probability of detecting a geoneutrino is called survival probability. The average two-flavor survival probabilities and an exact approach to matter-oscillations are used. Overall, the two-flavor case shows a good fit to other studies on signal prediction from the mantle but underestimates the total flux from the Earth, while the exact-solution approach overestimates the mantle signal and gives total-flux results within the limits of the observed geoneutrino fluxes provided by KamLAND and Borexino detectors. In spite of that, further testing on the software written for the exact-solution are to be performed to evaluate the implementation accuracy. So far, geoneutrinos have proven to be an useful tool to understand the chemical composition of the planet. However, the resolution of the detectors is a significant limitation; improvements in this matter are expected in the years to come.

Resumen

Los neutrinos son aún un tema enigmático en física debido a sus extrañas propiedades. No obstante, ha surgido un campo en Geociencia de Neutrinos, el cual usa estas propiedades únicas para estudiar la Tierra. En este proyecto se muestran los resultados de las simulaciones hechas para calcular la señal esperada de geoneutrinos (antineutrinos electrónicos provenientes de decaimiento beta natural) para distintas distribuciones de Elementos Productores de Calor (HPE) en el manto, así como diferentes modelos de Composición del Manto Primitivo (BSE). Se denomina probabilidad de supervivencia a la probabilidad de detectar un geoneutrino; para calcularla se utilizó la aproximación de dos sabores y una solución exacta para la oscilación en la materia. En general, el primer caso se ajusta a las predicciones de otros estudios para la señal del manto pero los resultados para el flujo de toda la Tierra son menores de lo esperado; mientras el segundo caso resulta en valores altos para la señal del manto y otorga, para el flujo total, resultados dentro de los límites dados por las observaciones de los detectores KamLAND y Borexino. A pesar de esto, son necesarias más pruebas sobre el software escrito para la solución exacta que tendrá como objetivo evaluar su precisión. Los geoneutrinos muestran ser de utilidad para el estudio de la composición química de la Tierra, sin embargo la resolución de los detectores es una limitante significativa; se esperan avances en este ámbito durante los próximos años.

Acknowledgements

I would like to acknowledge, in the first place, my parents and family, whose hard work and teaching have allowed me to get here.

Then, I acknowledge my advisors, who guided me through this project.

Also, thanks to my friends, who supported me even though they don't remember what this project is about.

Finally, thanks to the people at Stackoverflow, who taught me how to code.

Contents

| | | |
|----------|--|-----------|
| 1 | Introduction | 1 |
| 2 | Relevance of the Study | 3 |
| 3 | Distribution of Radioactive Elements | 5 |
| 3.1 | Distribution of Elements | 5 |
| 3.2 | Relative Abundances | 6 |
| 3.2.1 | Bulk Silicate Earth | 6 |
| 3.2.2 | Crust | 7 |
| 3.2.3 | Mantle | 8 |
| 4 | Radioactivity | 9 |
| 4.1 | Overview | 9 |
| 4.2 | Types of radioactive decay | 10 |
| 4.2.1 | Alpha decay | 10 |
| 4.2.2 | Gamma decay | 11 |
| 4.2.3 | Beta decay | 11 |
| 4.3 | Decay Chains | 13 |
| 4.4 | (Anti)Neutrino emission | 13 |
| 5 | Neutrino Physics | 15 |
| 5.1 | Neutrino interactions | 15 |
| 5.1.1 | Antineutrino detection: Inverse beta | 17 |
| 5.2 | Neutrino oscillations | 18 |
| 5.2.1 | Vacuum oscillations | 19 |
| 5.3 | Neutrinos in matter | 21 |
| 5.3.1 | MSW effect | 22 |
| 5.3.2 | Three-flavor MSW exact solution | 23 |

| | | |
|-------------------|--|-----------|
| 5.3.3 | Two-flavor approximation | 24 |
| 5.3.4 | Solar Neutrino Problem | 25 |
| 6 | The Model | 27 |
| 6.1 | Modeling the Earth | 27 |
| 6.2 | Modeling the Flux | 28 |
| 6.2.1 | The Flux Integral | 28 |
| 6.2.2 | Survival Probability | 29 |
| 6.3 | Terrestrial Neutrino Units | 30 |
| 7 | UANdINO | 33 |
| 7.1 | Path generation and number of steps | 33 |
| 7.2 | Optimization in steps: Skipping | 34 |
| 7.3 | Parallelization | 35 |
| 7.4 | Accuracy tests | 36 |
| 7.4.1 | Two-flavor neutrinos | 36 |
| 7.4.2 | Solar Neutrinos | 37 |
| 8 | Results | 38 |
| 8.1 | UANdINO | 38 |
| 8.2 | Flux simulation | 40 |
| 9 | Analysis | 45 |
| 10 | Conclusions | 49 |
| 10.1 | Further Directions | 50 |
| References | | 51 |
| Appendices | | |
| Appendix A | Graph reproduction | 55 |
| Appendix B | Dependence of P_{ee} on the path | 63 |

List of Figures

| | | |
|-----|--|----|
| 4.1 | Feynman diagram for β^+ process. | 11 |
| 4.2 | Feynman diagram for β^- process. | 12 |
| 4.3 | Feynman diagram for electron capture. | 12 |
| 4.4 | Geoneutrino energy spectrum. | 14 |
| 5.1 | QED vertex. | 17 |
| 5.2 | Charged-current (CC) interaction of leptons. | 17 |
| 5.3 | Neutral-current (NC) interaction of leptons. | 18 |
| 5.4 | Three-flavor survival probability in vacuum. | 21 |
| 5.5 | Some CC and NC interactions in matter. | 21 |
| 5.6 | Solar neutrino spectrum | 25 |
| 5.7 | Illustration of the solar neutrino problem | 26 |
| 6.1 | Model Earth | 28 |
| 6.2 | Attributes of class <code>RingNode</code> | 32 |
| 7.1 | Time-Steps relation | 34 |
| 7.2 | Neutrino survival probability for a step-function potential. | 36 |
| 7.3 | Survival probability for solar ν_e . Simulation vs. experiments | 37 |
| 8.1 | P_{ee} and path from node (1, 1) (diameter). | 39 |
| 8.2 | Energy-integrated P_{ee} 's for all paths in Earth from UAndINO. | 40 |
| 8.3 | HPE abundances and flux contribution in TL model. | 43 |
| 8.4 | HPE abundances and flux contribution in uniform model. | 44 |
| 9.1 | Mantle flux results. | 47 |
| 9.2 | Total flux results. | 48 |
| A.1 | Figure 1 reproduction | 56 |

| | | |
|------|---|----|
| A.2 | Figure 1 taken from reference [16] | 56 |
| A.3 | Figure 2 reproduction | 57 |
| A.4 | Figure 2 taken from reference [16] | 57 |
| A.5 | Figure 3 reproduction | 58 |
| A.6 | Figure 3 taken from reference [16] | 58 |
| A.7 | Figure 4 reproduction | 59 |
| A.8 | Figure 4 taken from reference [16] | 59 |
| A.9 | Figure 5 reproduction | 60 |
| A.10 | Figure 5 taken from reference [16] | 60 |
| A.11 | Figure 6 reproduction | 61 |
| A.12 | Figure 6 taken from reference [16] | 61 |
| A.13 | Figure 7 reproduction | 62 |
| A.14 | Figure 7 taken from reference [16] | 62 |
| B.1 | P_{ee} and path from node (1, 400) to the detector. | 64 |
| B.2 | P_{ee} and path from node (1, 800) to the detector. | 65 |
| B.3 | P_{ee} and path from node (1, 950) to the detector. | 66 |
| B.4 | P_{ee} and path from node (400, 400) to the detector. | 67 |

List of Tables

| | | |
|-----|---|----|
| 6.1 | Constants used. | 29 |
| 8.1 | Two-flavor approximation mantle flux results. | 41 |
| 8.2 | UANdINO mantle flux results. | 41 |
| 8.3 | Two-flavor approximation total flux results. | 42 |
| 8.4 | UANdINO total flux results. | 42 |
| 9.1 | Detector measurements. | 45 |
| A.1 | Two-flavor oscillation parameters. | 55 |

1

Introduction

“I have done something very bad today by proposing a particle that cannot be detected”

– Wolfgang Pauli

Fortunately, Pauli was a bit wrong in this one, not because of the prediction of the particle, but for the fact that we were, eventually, able to detect these particles called neutrinos. They have been proven to be some of the most bizarre mysteries of our universe due to their unique physical behavior and properties. Their low interaction and oscillation phenomena makes them, not only difficult to see, but also useful in some areas of study. The present work focus on how can we exploit these characteristics to get useful information of some physically unreachable places, for example, the Earth’s interior.

In this work, I will be simulating the geoneutrino flux from an azimuthally symmetrical Earth, taking into account the PREM density model [5]. This simple Earth’s structure model plus the usage of an exact solution for the antineutrino oscillation in the matter [16] make a “simple enough” model of the problem that will allow to draw some conclusions on the Heat Producing Element distribution in the mantle and evaluate the usefulness of the complete, exact treatment of neutrino oscillations in this context.

The second chapter briefly describes the relevance of this study. Then, the distribution of radioactive elements in the Earth is discussed, first, through an overview of the Goldschmidt classification of chemical ele-

ments, and then, showing the abundances of the relevant isotopes in each of the three main layers of the planet.

In chapter 4 the phenomenon of radioactivity is explained, as well as the different types of radioactive decay. The relevant decay chains are shown, along with the geoneutrino spectra for the β^- decay.

Chapter 5 is an overview of neutrino physics. This includes a short description of the oscillation phenomena, a little discussion on neutrino interactions, the MSW effect, as well as introducing two different methods of calculating the survival probability for an electron (anti)neutrino: the exact, three-flavor matter oscillation used in this study and the two-flavor matter oscillation used in some previous studies. Finally a small presentation of the Solar Neutrino Problem is given.

Then, in chapter 6, the details of the modeling, including some aspects of the programs written, are given. This is considered a crucial part of this work as it will be the base of any further study to be done.

The chapter 8, presents the results of the simulations, while in chapter 9 they are discussed. Finally, in chapter 10 some conclusions on this project are given, as well as the further directions on the field.

2

Relevance of the Study

The Earth is a complex system, in which we are rarely able to directly probe some characteristics, such as the composition of the deep Earth. In this aspect, one usually uses the available information in the surface, such as the composition of xenoliths or geophysical surveys like gravity or seismics, which are directly related to rheology and other physical characteristics of the rock, from which some relations to the composition can be withdrawn. Inspired by the latter, we can say that the development of indirect methods to probe the deep Earth is important, given the impossibility of directly doing it.

Neutrino geoscience is a relatively new field in geophysics and some applications of it are the estimation of radiogenic heat flux (Urey ratio) and testing HPE distributions or BSE models, nevertheless, being a new field as it is, the full potential of neutrino geoscience is yet to be discovered. Nevertheless, this new field should be able complementary to usual deep Earth exploration methods like seismics and gravity since (anti)neutrinos are only affected by the electron density, which is directly related to the chemical composition; while the usual geophysical methods can probe characteristics that are an input to (anti)neutrino studies, in order to further improve our knowledge of the planet.

In order to develop reliable studies that involve (anti)neutrino oscillations through different variable densities, the appropriate computational tools must be developed. Thus, this study includes the development of UANdINO, the Uniandes ANtineutrINO Oscillation calculator. This is a

2. RELEVANCE OF THE STUDY

GSL (reference [8]) based software dedicated to provide an exact calculation of transition and survival probabilities for a(n) (anti)neutrino, with energy E_ν , traveling through a varying density path. Along with it, other side programs were developed for modeling the Earth's structure.

3

Distribution of Radioactive Elements

3.1 Distribution of Elements

A first, basic approach to understanding the distribution of elements in the Earth was given by Goldschmidt [10], who developed a classification system for the chemical elements. This classification is, in a nutshell, *lithophile* or oxygen-loving elements tend to remain in the uppermost part of the solid planet; *siderophile* or iron-loving elements, tend to be close to the nucleus and are not attracted to oxygen, unlike the lithophiles. The *chalcophile* elements are sulfur-loving and, thus, do not like the deep Earth. Finally, the *atmophile* elements are those who like to be in the atmosphere.

There are many radioactive isotopes in the Earth, which are, basically, atoms so heavy that they are unstable, and go through different processes to reach a more stable state. This will be the topic of chapter 4. Most of these heavy elements are classified as lithophiles. We are particularly interested in some isotopes that dominate the geoneutrino production (99% of production) [13], these are ^{40}K , ^{235}U , ^{238}U and ^{232}Th .

Within each of the groups given by Goldschmidt and briefly described here, there is other classification that discriminates elements based on their condensation temperature. The elements with a high value of this parameter are called *refractory* while the ones with a lower one are called *volatile*.

Let us then picture the scenario of the formation of the Earth. About 4500 *Gyr* ago, the solar system and the Earth were being formed, the latter through planetary accretion, this means, a hot, undifferentiated mass of molten rock that is slowly cooling down, the consequences of this are, first of all, density differentiation, that causes the heavier elements to accumulate near the center of mass, thus, forming the nucleus. It also causes the elements to condense, so the refractory ones, are quickly trapped into the Earth, making it possible to infer the initial abundances of these elements in the primitive Earth by looking at their abundances in different meteorites. On the other hand, volatile elements will not be trapped so easily or quickly, instead, there is a possibility that these elements have escaped the primitive Earth while it was hotter; the gases are extremely volatile, while there are other elements, like potassium (whose relevance will become obvious in the following sections) that are moderately volatile.

I have mentioned that the cooling down of the primitive Earth, lead to density differentiation in layers, causing the layered structure of the planet. The less-dense melt that ascended all the way up made up the crust, and is enriched in lithophile elements such as *U*, *Th*, *K*. Nevertheless, there is still a large amount of these elements in the mantle.

3.2 Relative Abundances

This section is devoted to discuss the different views on the distribution of the radioactive isotopes, in depth, quantitatively. There are two main discussions to be considered; first, the average composition of the Bulk Silicate Earth (BSE) and, second, the distribution of Heat Producing Elements (HPE) in the mantle.

3.2.1 Bulk Silicate Earth

In the first place, we shall define the BSE as the “average” Earth composition when excluding the nucleus, in other words, an average between mantle and crust. Three main ideas on the BSE composition have arisen through the years and each one of them relies on different, valid, arguments.

The first model is the *geochemical*, that as the name suggests, is based in geochemical arguments to give values to the abundances and abundance ratios of elements in the planet. McDonough [14] analyzed peridotite samples in order to infer the BSE average compositions. Reference [14] reports values of $A_{Th}^{BSE} = 79.5 \text{ ppb}$, $A_K^{BSE} = 240 \text{ ppm}$ and $A_U^{BSE} = 20.3 \text{ ppb}$, while reference [21] reports $A_{Th}^{BSE} = 80 \pm 13 \text{ ppb}$, $A_K^{BSE} = 280 \pm 60 \text{ ppm}$ and $A_U^{BSE} = 20 \pm 4 \text{ ppb}$ for this BSE model, note that both references are in agreement. A_X^Y stands for the abundance of element X in reservoir Y .

The second model is the *geodynamical*. This model is based on the current measurements of the Earth's heat flow and assumes that the fraction of this heat due to radioactive decay is higher than the fraction due to secular cooling of the planet. In reference [21], the reported values of the abundances are $A_{Th}^{BSE} = 140 \pm 14 \text{ ppb}$, $A_K^{BSE} = 350 \pm 35 \text{ ppm}$ and $A_U^{BSE} = 35 \pm 4 \text{ ppb}$. This model has particularly high values of A_X^Y due to the assumption that the majority of the flux is product of radioactivity.

The third and final model is the *cosmochemical*. It relies on the analysis of enstatite chondrites to infer the BSE composition, under the argument that this abundances specially the iron one, will easily explain the presence of the core, as explained in reference [13]. Reference [21] reports the following values relevant to this project: $A_{Th}^{BSE} = 43 \pm 4 \text{ ppb}$, $A_K^{BSE} = 146 \pm 29 \text{ ppm}$ and $A_U^{BSE} = 12 \pm 2 \text{ ppb}$.

In this study, I will compare the results for geoneutrino measurements for the different BSE models presented above.

3.2.2 Crust

The relative abundance of HPE in the crust has been the object of various studies ([11, 15, 18, 22, 24]) among which, for this project, I chose reference [11]. In this article, the authors develop a reference Earth model for the HPE, based on geochemical analysis performed on different rocks and following the CRUST 2.0 model for crustal thickness and properties. The values given are $A_U^C = 453.19_{-0.25}^{+0.29} \text{ ppb}$ and $A_{Th}^C = 1940.64_{-0.89}^{+1.56} \text{ ppb}$.

3.2.3 Mantle

The abundance of isotope X in the mantle, A_X^M , is calculated from the values reported above for A_X^{BSE} and A_X^C and the mass balance [21]:

$$m_{BSE}A_X^{BSE} = m_C A_X^C + m_M A_X^M, \quad (3.1)$$

that is, the total mass of isotope X is the sum of the mass in the crust and the mantle. The mass of reservoir Y , m_Y , is calculated through integration of the mass density of the Earth given by the PREM model in reference [5], the details of the method will be given in chapter 6.

Additionally, the mantle structure is currently debated. Two of the most accepted models are the uniform mantle and the two-layer (EL-DL) mantle. The former consists in uniformly distributed HPE over the mantle, thus, the abundance in every point will be given by equation 3.1. The latter, in which EL and DL stand for enriched and depleted layer, respectively, consists in two layers of slightly different HPE abundances. The enriched layer is said to constitute the lowermost 10% in mass of the bulk mantle [21]. The abundance in these two layers is also calculated using a relation similar to equation 3.1. The motivation for this is that the difference between the types of basalts (OIB, MORB, etc.) is thought to be caused by the differentiation of the mantle into two chemically distinct layers, an enriched layer and a depleted one, respect to lithophile elements.

4

Radioactivity

4.1 Overview

Radioactivity is the phenomenon in which a parent isotope turns into a daughter isotope, with different characteristics, through the emission of a particle.

The history of radioactivity goes back to 1896, when H. Becquerel discovered that a uranium sample emitted some kind of penetrating radiation similar to the X rays (discovered earlier that year). In the following years, three different types of emissions were identified: alpha (α), beta (β) and gamma (γ). The nature of each of these emissions was identified through the years, concluding that α -particles correspond to 4He nuclei, β^\pm -particles correspond to e^\pm (electrons or positrons) and γ -particles are nothing but high energy photons.

Rutherford discovered that radioactive phenomena was linked directly with the nucleus (size $\sim 1 \text{ fm}$) of a given isotope, thus, it had to be an entirely quantum phenomenon.

The overall radioactive phenomena are described by a rather simple mathematical approach given its statistical behavior (which is a result, and evidence of how “quantum” it is). Given N parent isotopes in a sample at a certain time t and assuming no more are added, the rate of

decay (dN/dt) is proportional to N [12]

$$\frac{dN}{dt} = -\lambda N \quad (4.1)$$

That, upon integration, becomes

$$N(t) = N_0 \exp(-\lambda t) \quad (4.2)$$

Where N_0 corresponds to the number of parent isotopes at time $t = 0$ and λ is called the decay constant and is unique for every isotope.

This simple model has been key to the use of the radioactive isotopes to, for example, date rocks or organisms [12].

4.2 Types of radioactive decay

Let us now go deeper into the theory of the radioactivity, that is, briefly describe the different types of radioactive decays since not all of them produce antineutrinos, and these are the particles that concern this text.

4.2.1 Alpha decay

The theory of the alpha decay is rather simple. The α -particles are confined in a finite potential well (the nucleus X) and will, as expected, have a certain probability of tunneling through it. When this happens, the α -particle will escape and leave a “new” (daughter) nucleus X' [12]. The process may be written as



Where A is the atomic mass number, Z is the atomic number and N is the number of neutrons.

This decay involves both strong (nuclear) interactions and electromagnetic interactions since the potential well is given by confinement due to strong interaction between nucleons and the barrier has a decaying-exponential side, given by the Coulomb potential.

4.2.2 Gamma decay

Gamma decay is similar to the common electromagnetic emission due to atomic transitions, in fact, it is produced when a metastable state of an isotope decays into a more stable one through the emission of high energy photons. It should be noted that, in this case, no change in A or N is produced. These metastable states are common daughter isotopes to α and β decays.

Lifetimes for this kind of process is generally short, taking only fractions of a second to decay while some α -decaying isotopes may have half-lives of the order of 10^3 yr.

4.2.3 Beta decay

This type of decay can be considered to be more complex than the other two, as it responds to more complicated underlying physics: the weak interaction. It consists in a set of semileptonic processes (that involve both leptons and hadrons) that will be described below.

- Positive Beta decay:

$$p \rightarrow n + e^+ + \nu_e \quad (4.4)$$

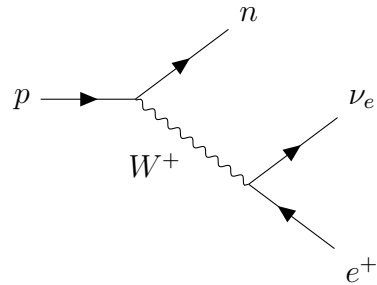


Figure 4.1: Feynman diagram for β^+ process.

- Negative Beta decay:

$$n \rightarrow p + e^- + \bar{\nu}_e \quad (4.5)$$

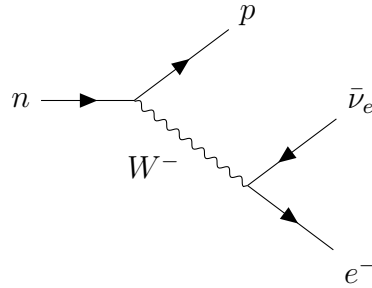


Figure 4.2: Feynman diagram for β^- process.

- **Electron capture:**

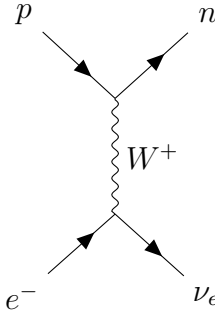


Figure 4.3: Feynman diagram for electron capture.

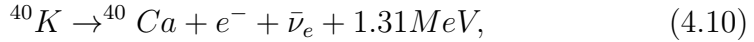
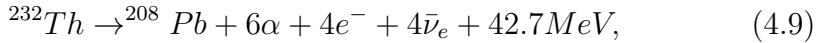
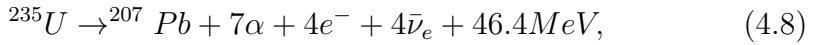
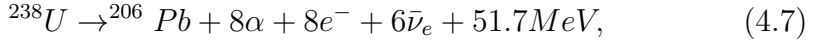
Note that in all these processes new particles are created in the nucleus, which is a consequence of the weak interaction that rules them.

The particles labeled with ν_e are electron neutrinos and were proposed by Pauli in order to solve the conundrum concerning the apparently continuous energy spectra of β -decay which is against the core of quantum mechanics; the inclusion of these particles in the energy spectrum of the decay made it discrete, thus, giving a solution to the problem [9].

For this project, we are strictly interested in the β^- -decay since it is the one that produces antineutrinos.

4.3 Decay Chains

Different isotopes in the Earth have decay chains that involve β^- -decay at some point, but there are a few ones that dominate the antineutrino production. The reader may have noticed that in chapter 3, I have said that the production of heat is dominated by ^{238}U , ^{232}Th and ^{40}K . Each isotope has a decay chain that includes some beta decays. These are summarized in the following equations.



Note that the processes shown in equations 4.10 and 4.11 have the same parent isotope, the former happens with a probability of 89.3% and the latter with the remaining 10.7%.

In equations 4.7 through 4.11, the particles $\bar{\nu}_e$ are electron antineutrinos, also called geoneutrinos, in this context.

4.4 (Anti)Neutrino emission

As seen in the previous section, naturally produced antineutrinos from beta decay are called geoneutrinos. These are produced following a given spectrum [7], shown in figure 4.4.

Figure 4.4 shows that the energy domain for these particles is relatively low, this means that, in the light of reference [16], oscillations might not be of such importance because the transition and survival probabilities do not show a clear pattern in these energy scales. In fact they seem to oscillate with a really low period and amplitude around a certain value, so the

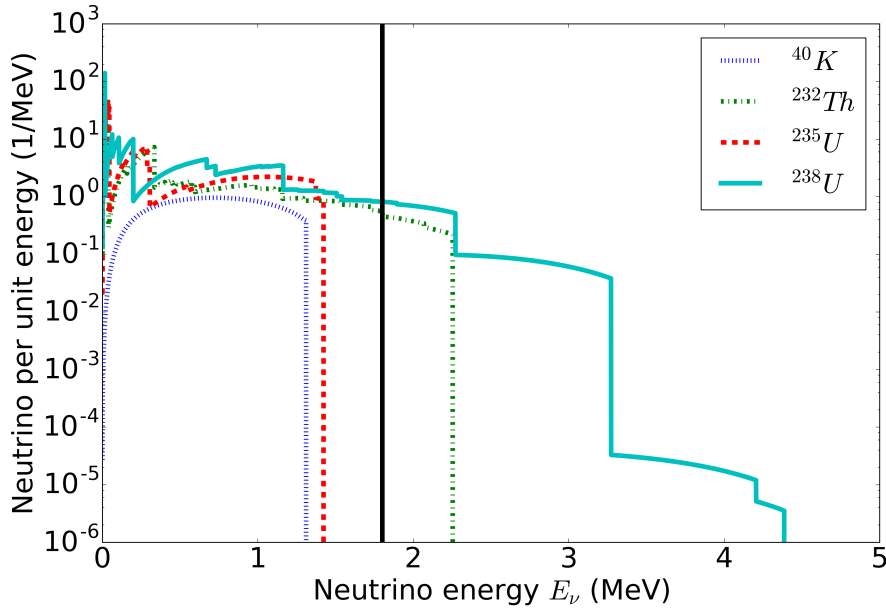


Figure 4.4: Geoneutrino energy spectrum from [7]. The vertical line, is the kinematic threshold energy $E_\nu = 1.8$ MeV briefly discussed in section 5.1.1.

oscillation itself seems to have little effect on the average probability. But this effect and its influence is what this project aims to study. Nevertheless it is worth mentioning that resonances in the probabilities are present at higher energy scales, which may be useful in neutrino geoscience if one is using “extraterrestrial” neutrinos instead of geoneutrinos since these may have higher energies.

5

Neutrino Physics

This chapter is only an overview of the special physics that surrounds these particles, for a thorough explanation you should see reference [9] and for details on time evolution, reference [16].

Neutrinos are neutral leptons that interact weakly and are always produced in a flavor eigenstate $|\nu_\alpha\rangle$ with $\alpha = e, \mu, \tau$. In equations 4.4 to 4.6, all neutrinos are labeled ν_e that stands for electron neutrino, this is because they are all associated with the “ordinary” matter which is composed by electrons, not tauons (τ) nor muons (μ), which are other charged leptons, this is, electrically charged particles that lack color charge.

5.1 Neutrino interactions

We have mentioned that neutrinos interact weakly, in fact, the weak interaction is the *only* one they participate in, since they lack both electric and color charge.

The weak interaction is the weakest among the fundamental interactions: electromagnetic, strong, weak and gravitational. It is mediated by three massive vector bosons, two of them charged, W^\pm and one neutral, Z^0 . The weak processes are divided in 3:

- **Leptonic processes:** Only leptons are involved.

$$\mu^- \rightarrow e^- + \bar{\nu}_e + \nu_\mu \quad (5.1)$$

$$\nu_e + e^- \rightarrow \nu_e + e^- \quad (5.2)$$

$$\nu_\mu + e^- \rightarrow \nu_e + \mu^- \quad (5.3)$$

- **Semileptonic processes:** Both hadrons and leptons are involved.

$$\pi^+ \rightarrow \pi^0 + e^+ + \nu_e \quad (5.4)$$

$$n \rightarrow p + e^- + \bar{\nu}_e \quad (5.5)$$

$$\Sigma^0 \rightarrow \Lambda^0 + e^- + \bar{\nu}_e \quad (5.6)$$

$$\bar{\nu}_e + p \rightarrow e^+ + n \quad (5.7)$$

⋮

- **Hadronic processes:** Only hadrons are involved.

If we wish to formally describe these interactions, we have to build a gauge theory for the electroweak interaction, that is, for symmetry group $SU(2)_L \times U(1)_Y$. L stands for *left-handed chirality* and Y for *weak hypercharge*. We are, in this case, not interested in the details of the theory, however, the biggest takeout relevant to this discussion is the interaction lagrangian

$$\mathcal{L}_I = -j_{EM}^\mu A_\mu - \frac{g}{2\sqrt{2}}(j^{\mu\dagger} W_\mu + j^\mu W_\mu^\dagger) - \frac{g}{\cos \theta_w} j_0^\mu Z_\mu, \quad (5.8)$$

with coupling constant g and θ_w , the Weinberg angle.

The first term describes the coupling between an electromagnetic current for a *charged* lepton l [19]

$$j_{EM}^\mu = -e\bar{\psi}_l \gamma^\mu \psi_l \quad (5.9)$$

and the EM field A_μ . This interaction is, therefore, the QED vertex shown in figure 5.1.

The second term is the interaction between *charged* currents

$$j^\mu = \bar{\psi}_l \gamma^\mu (1 - \gamma_5) \psi_l \quad (5.10)$$

$$j^{\mu\dagger} = \bar{\psi}_{\nu_l} \gamma^\mu (1 - \gamma_5) \psi_l \quad (5.11)$$

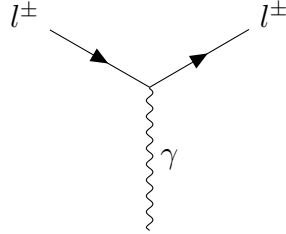


Figure 5.1: QED vertex.

and a field

$$W^\mu = \frac{1}{\sqrt{2}}(W_1^\mu - iW_2^\mu), \quad (5.12)$$

where τ_i is the i -th Pauli matrix. This coupling is shown as the diagram in figure 5.2.

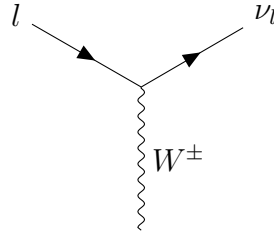


Figure 5.2: Charged-current (CC) interaction of leptons.

The last term gives us the interaction between the *neutral* current (NC)

$$j_0^\mu = \frac{1}{4}(\bar{\psi}_{\nu_l} \gamma^\mu (1 - \gamma_5) \psi_{\nu_l} - \bar{\psi}_l \gamma^\mu (1 - 4 \sin^2 \theta_w - \gamma_5) \psi_l) \quad (5.13)$$

and the Z_μ field. Figure 5.3 shows the diagrams for both terms in the NC.

5.1.1 Antineutrino detection: Inverse beta

Current experiments such as KamLAND and Borexino detect antineutrinos through inverse beta process



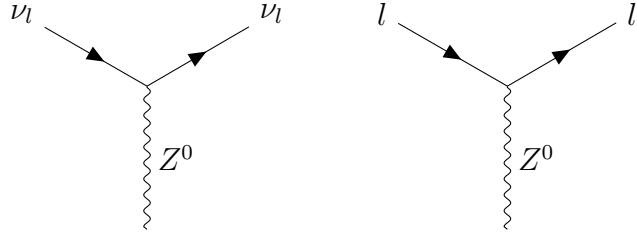


Figure 5.3: Neutral-current (NC) interaction of leptons.

Protons are those of the hydrogen in the hydrocarbon scintillator within the detector.

The detection signature consists in the annihilation of the positron plus the neutron capture and the fact that these events are time-correlated [13]. The threshold energy for the process in equation 5.14 is given by

$$E_{min} = \frac{m_n^2 + m_e^2 - m_p^2 + 2m_n m_e}{2m_p} = 1.8 \text{ MeV}, \quad (5.15)$$

so antineutrinos with $E_\nu < E_{min}$ are not detected.

5.2 Neutrino oscillations

One should note that all interactions mentioned in the previous section involve (anti)neutrinos with a given *flavor*. These flavors are electron, tau and muon neutrinos (ν_e , ν_τ , ν_μ respectively).

Flavor eigenstates are *not* energy eigenstates. Since quantum mechanics dictates that the time evolution of a quantum system is entirely determined by the Hamiltonian, neutrinos will not travel (evolve) in a flavor eigenstate but in a mass (energy) eigenstate.

We can write a flavor state, $|\nu_\alpha\rangle$, as a linear combination of the mass ones, $|\nu_a\rangle$, $a = 1, 2, 3$,

$$|\nu_\alpha\rangle = \sum_{a=1}^3 U_{\alpha a}^* |\nu_a\rangle, \quad (5.16)$$

where the coefficients $U_{\alpha a}^*$ are the matrix elements of the transformation matrix U^* [16].

The matrix U^* is the complex conjugate of matrix U , called Pontecorvo-Maki-Nakagawa-Sakata (PMNS) matrix, that rules the mixing of the neutrinos and can be parametrized as shown in reference [16]:

$$U = \begin{bmatrix} C_{13}C_{21} & S_{21}C_{13} & S_{13} \\ -S_{13}C_{23} - S_{23}S_{13}C_{12} & C_{23}C_{12} - S_{23}S_{13}S_{12} & S_{23}C_{13} \\ S_{23}S_{12} - S_{13}C_{23}C_{12} & -S_{23}C_{12} - S_{13}S_{12}C_{23} & C_{23}C_{13} \end{bmatrix}, \quad (5.17)$$

where $S_{ij} \equiv \sin(\theta_{ij})$ and $C_{ij} \equiv \cos(\theta_{ij})$. Parameters θ_{ij} are the vacuum mixing angles, defined by $\sin^2 \theta_{23} = 0.437$, $\sin^2 \theta_{13} = 0.0214$ and $\sin^2 \theta_{12} = 0.297$ in reference [17]. Here we have assumed there is no charge-parity (CP) phase, thus, $U = U^*$.

5.2.1 Vacuum oscillations

We can only see interactions in flavor eigenstates, so to us, the neutrinos will oscillate between them while traveling, this is, there is a probability $P_{\alpha\beta} \neq 0$ that the neutrino produced in flavor eigenstate β is detected in state α .

According to the principles of quantum mechanics, the Hamiltonian of a system described by the ket $|\psi\rangle$ defines its time evolution according to

$$|\psi(t)\rangle = \exp(-i\hat{H}(t-t_0))|\psi(t_0)\rangle \quad (5.18)$$

In the case of the neutrinos, we know that they do not travel in flavor state but in mass states, then, we can write

$$|\nu_a(t)\rangle = \exp(-i\hat{H}_m(t-t_0))|\nu_a(t_0)\rangle = \hat{U}_m(t-t_0)|\nu_a(t_0)\rangle. \quad (5.19)$$

In mass basis, the Hamiltonian will be diagonal

$$\hat{H}_{m,0} = \begin{bmatrix} E_1 & 0 & 0 \\ 0 & E_2 & 0 \\ 0 & 0 & E_3 \end{bmatrix}, \quad (5.20)$$

so the evolution will be

$$|\nu_a(t)\rangle = \exp(-iE_a(t-t_0))|\nu_a(t_0)\rangle. \quad (5.21)$$

If we substitute expression 5.21 in equation 5.16, we get

$$|\nu_\alpha(t)\rangle = \sum_\beta \sum_a U_{\alpha a}^* \exp(-iE_a(t-t_0)) U_{\beta a} |\nu_\beta(t_0)\rangle. \quad (5.22)$$

We can now define the time-evolution operator in flavor basis

$$(\hat{U}_f(t-t_0))_{\alpha\beta} = \sum_a U_{\alpha a}^* \exp(-iE_a(t-t_0)) U_{\beta a} \quad (5.23)$$

We can now make the substitution $L \approx ct$, $c = 1$, the speed of light. This is because (anti)neutrinos are extremely light and, thus, travel at a speed *very* close to c .

Then, the transition probability from an initial flavor α state to a β after traveling a distance $L = t - t_0$ will be

$$P_{\alpha \rightarrow \beta} = |\langle \beta | \hat{U}_f(L) | \alpha \rangle|^2 = |(\hat{U}_f(L))_{\alpha\beta}|^2. \quad (5.24)$$

In this case, we get

$$P_{\alpha \rightarrow \beta} = \sum_a \sum_b U_{\alpha a}^* U_{\alpha b} \exp(-i(E_a - E_b)L) U_{\beta a} U_{\beta b}^*. \quad (5.25)$$

We can now define, in the ultrarelativistic limit $v \approx c$

$$E_{ab} = E_a - E_b \approx \frac{\Delta m_{ab}^2}{2E_\nu}, \quad (5.26)$$

where $\Delta m_{ab}^2 \equiv m_a^2 - m_b^2$ is the *squared-mass-difference* between mass eigenstates a and b . The latest values for these parameters provided in reference [17] are $\Delta m_{21}^2 = 7.37 \times 10^{-5}$ eV² and $\Delta m_{32}^2 = 2.54 \times 10^{-3}$ eV². Finally, we get

$$P_{\alpha \rightarrow \beta}(L) = \sum_a \sum_b U_{\alpha a}^* U_{\alpha b} \exp\left(-i \frac{\Delta m_{ab}^2}{2E_\nu} L\right) U_{\beta a} U_{\beta b}^*. \quad (5.27)$$

If we wish to calculate the survival probability, this formula reduces, according to reference [13], to

$$P_{ee} = \sin^4 \theta_{13} + \cos^4 \theta_{13} \left(1 - \sin^2 2\theta_{12} \sin^2 \left(\frac{1.267 \Delta m_{21}^2 L}{4E_\nu} \right) \right). \quad (5.28)$$

The survival probability in this context is shown in figure 5.4.

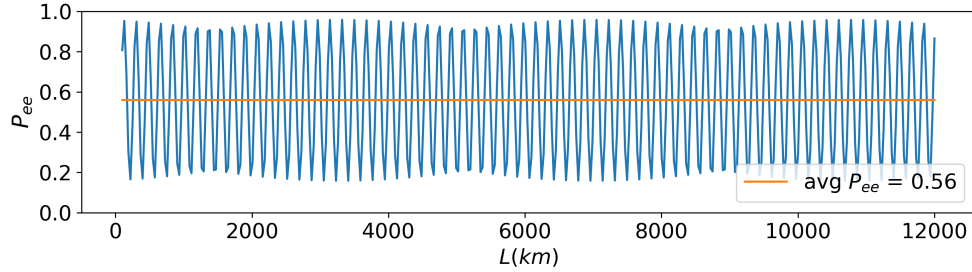


Figure 5.4: Survival probability in function of the distance to the detector obtained through the three-flavor vacuum solution (Eq. 5.28, $E_\nu = 10^6 \text{ eV}$).

5.3 Neutrinos in matter

When propagating through matter, neutrinos are subject to the interactions previously described, the processes involved are shown in figure 5.5. Both of them generate an effective potential term in the Hamiltonian, al-

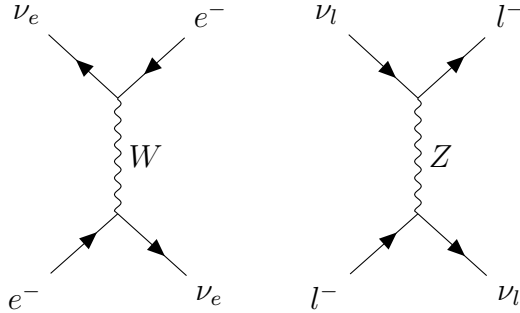


Figure 5.5: Some CC and NC interactions in matter.

though, the NC potential can be neglected as its contribution is the same for all flavors and thus, does not affect the transition probabilities [9]. The effective potential is, in flavor basis,

$$\hat{V}_f = \mathcal{A} \begin{bmatrix} 1 & 0 & 0 \\ 0 & 0 & 0 \\ 0 & 0 & 0 \end{bmatrix}, \quad (5.29)$$

where \mathcal{A} depends on the density of the matter the neutrino is going through, and is defined as

$$\mathcal{A}(r) = \sqrt{2}G_F N_e(r) \approx \pm \frac{1}{\sqrt{2}} G_F \frac{\rho(r)}{m_N}. \quad (5.30)$$

Here, G_F is the Fermi coupling constant, $N_e(r)$ is the electron density, $\rho(r)$ is the matter density and m_N is the nucleon mass. This quantity is $\mathcal{A} > 0$ for neutrinos and $\mathcal{A} < 0$ for antineutrinos.

Notice that this effective potential only affects the electron flavor hence, it will affect the oscillations in a non-trivial way, this is the Mikheyev-Smirnov-Wolfenstein (MSW) effect.

5.3.1 MSW effect

Following the explanation in reference [9], we will work, for now, in the two-flavor approximation. In this case, we may write the Hamiltonian of the system (as explained in [7])

$$\hat{H}_m = \begin{bmatrix} E_1 & 0 \\ 0 & E_2 \end{bmatrix} + U^{-1} V_f U, \quad U = \begin{bmatrix} \cos \theta & \sin \theta \\ -\sin \theta & \cos \theta \end{bmatrix}, \quad (5.31)$$

These results in a perturbed hamiltonian of the form

$$\hat{H}_f = \begin{bmatrix} -\frac{\Delta m^2}{4E_\nu} \cos 2\theta + \mathcal{A} & \frac{\Delta m^2}{4E_\nu} \sin 2\theta \\ \frac{\Delta m^2}{4E_\nu} \sin 2\theta & \frac{\Delta m^2}{4E_\nu} \cos 2\theta \end{bmatrix} \quad (5.32)$$

In order to solve this matter oscillation case, a new U' matrix is proposed

$$U' = \begin{bmatrix} \cos \theta' & \sin \theta' \\ -\sin \theta' & \cos \theta' \end{bmatrix}, \quad (5.33)$$

where

$$\cos 2\theta' \equiv \frac{-2\mathcal{A}E_\nu/\Delta m^2 + \cos 2\theta}{\sqrt{(2\mathcal{A}E_\nu/\Delta m^2 - \cos 2\theta)^2 + \sin^2 2\theta}}, \text{ and} \quad (5.34)$$

$$\sin 2\theta' \equiv \frac{\sin^2 2\theta}{\sqrt{(2\mathcal{A}E_\nu/\Delta m^2 - \cos 2\theta)^2 + \sin^2 2\theta}} \quad (5.35)$$

Then, the mass difference is

$$\Delta m'^2 = \sqrt{(2\mathcal{A}E_\nu - \Delta m^2 - \cos 2\theta)^2 + (\Delta m^2)^2 \sin^2 2\theta}. \quad (5.36)$$

The survival probability in this approximation is then

$$P_{ee} = 1 - \sin^2 2\theta' \sin^2 \left(\frac{\Delta m'^2 L}{4E_\nu} \right). \quad (5.37)$$

If we calculate

$$\tan 2\theta' = \frac{\sin^2 2\theta}{-2\mathcal{A}E_\nu/\Delta m^2 + \cos 2\theta}, \quad (5.38)$$

it is evident that there is maximal mixing when

$$\mathcal{A} = \frac{\Delta m^2 \cos 2\theta}{2E_\nu} \equiv \mathcal{A}_R. \quad (5.39)$$

The resonance at \mathcal{A}_R allows for total transitions between the two flavors, this is the MSW effect. For instance, in the Earth, where $\mathcal{A} \sim 10^{-13} eV$, we can expect resonances at $E_\nu \sim 10^4 MeV$ due to the “big” mass difference $\Delta m_{32}^2 \sim 10^{-3}$. The other mass difference $\Delta m_{21}^2 \sim 10^{-5}$ should produce resonances at $E_\nu \sim 10^2 MeV$. In any case, we should expect that, three-flavor mixing, leads to two resonances at energies such that $E_\nu^{R1}/E_\nu^{R2} \sim \Delta m_{32}^2/\Delta m_{21}^2$.

5.3.2 Three-flavor MSW exact solution

When considering three neutrino flavors, the matter-perturbed Hamiltonian, in mass basis is

$$\hat{H}_m = \begin{bmatrix} E_1 & 0 & 0 \\ 0 & E_2 & 0 \\ 0 & 0 & E_3 \end{bmatrix} + U^{-1}V_f U \quad (5.40)$$

Introducing equation 5.40 into 5.19 we can get the time evolution operator \hat{U}_f as follows (reference [16]).

Consider a $N \times N$ matrix M , the exponential of the matrix is defined as $\exp M = \sum_{n=0}^{\infty} \frac{1}{n!} M^n$. Now, recall Cayley-Hamilton’s theorem: given a matrix M , the characteristic polynomial is $p(x) = \det(x - M) = \sum_{i=0}^N c_i x^i$ ($c_N = 1$, $p(x)$ is monic), the theorem implies that $p(M) = 0$, this means that

$$p(M) = 0 = M^N + c_{N-1}M^{N-1} + \cdots + c_0, \quad (5.41)$$

then,

$$M^N = -c_{N-1}M^{N-1} - \cdots - c_0, \quad (5.42)$$

therefore, if one wishes to calculate M^m for any $m \geq N$, it will be given by

$$M^m = k_{N-1}^{(m)}M^{N-1} + \cdots + k_0^{(m)}, \quad (5.43)$$

given that coefficients $k_i^{(m)}$ are properly calculated. Knowing this, the exponential of the matrix

$$\exp M = \sum_{n=0}^{\infty} \frac{1}{n!} M^n = \sum_{n=0}^N a_n M^n \quad (5.44)$$

and this result is exact.

Given a density profile $\rho(\mathbf{r})$ over a region of total length L_T , one can divide it into K steps of length L_i , such that $L_T = KL_i$, with constant ρ_i ($\sim \mathcal{A}_i$). For each step, we could calculate the respective time evolution operators $\hat{U}_f(L_i)$ ($i = 0, \dots, K$) and build a total operator

$$\hat{U}_f(L_T) = \prod_{i=1}^K \hat{U}_f(L_i, \mathcal{A}_i), \quad (5.45)$$

that allows us to calculate the transition or survival probability through the relation 5.24.

5.3.3 Two-flavor approximation

Previous studies ([7, 13]) use the, already explained, two-flavor approximation to neutrino oscillation. This takes into account that the τ neutrino is so heavy that it is rarely produced. These references argue that the survival probability (equation 5.37) is well averaged since the oscillation distance $L_{osc} = \pi \frac{4E_\nu}{\Delta m^2} \ll R_{Earth}$. This results in very “tight” oscillations (similar to those illustrated in figure 5.4), for the Earth. Then,

$$\langle P_{ee} \rangle = 1 - \frac{1}{2} \sin^2 2\theta' = 0.56. \quad (5.46)$$

Notice that the frequency $\frac{\Delta m'^2 L}{4E_\nu}$ of $P_{ee}(E_\nu)$ will increase as E_ν decreases. This increase is, probably, the cause of the problems, at low energy, discussed in section 7.1.

5.3.4 Solar Neutrino Problem

The Sun is a neutrino generator. Equations 5.47 through 5.54 show the processes that produce them [6]. Figure 5.6 shows the spectra of these processes.

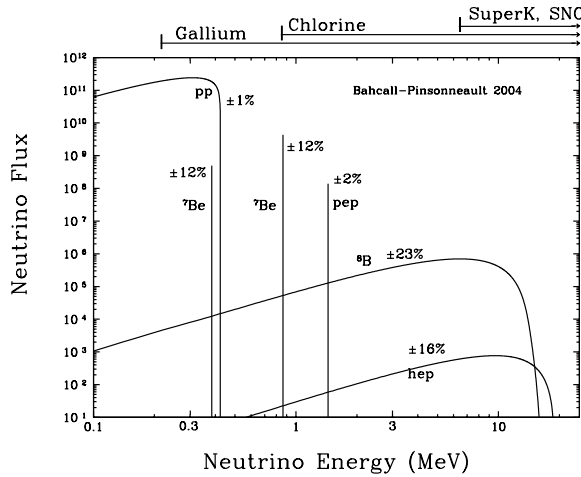
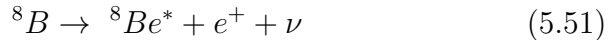
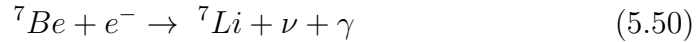


Figure 5.6: Solar neutrino spectrum and detection limits for different experiments. Taken from reference [3].

Different experiments have aimed at measuring the neutrino flux from the Sun. All solar neutrino detectors noticed a deficit in the measured quantity when compared to the Standard Solar Model (SSM) predictions.

The Sudbury Neutrino Observatory (SNO) predicted, for the process in equation 5.51, a flux of $5.69 \text{ cm}^{-2}/\mu\text{s}$ but the flux corresponding to detection through CC process was $1.68 \text{ cm}^{-2}/\mu\text{s}$ [6], about 30% of the expected flux. This “missing flux” is the *Solar Neutrino Problem*. Figure 5.7 shows the differences between theory and measurements for different experiments.

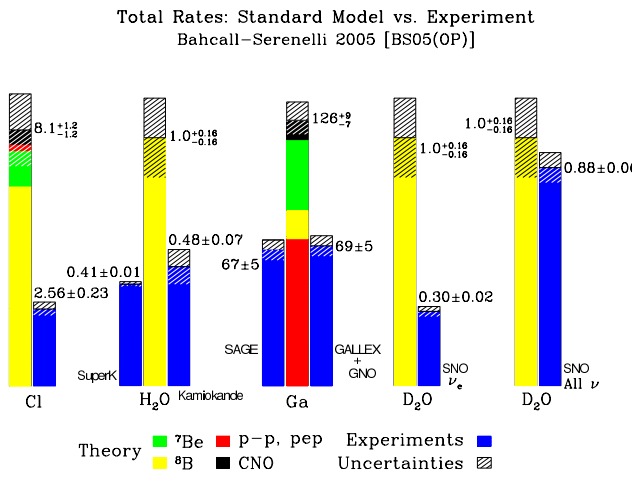


Figure 5.7: Illustration of the solar neutrino problem. Predicted fluxes vs. measurements for different experiments. Taken from reference [2].

The solution to this puzzle was, precisely, the MSW phenomenon. The Sun’s density profile is such that the effective potential felt by the electron neutrinos is $\mathcal{A}_{Sun} \sim 10^{-11} \text{ eV}$ then, a rough calculation of E_ν such that $\mathcal{A}_R \simeq \mathcal{A}_{Sun}$ (equation 5.39) gives us $E_\nu \sim 1 \text{ MeV}$ for the smaller squared-mass-difference, while the larger one causes a resonance in $E_\nu \sim 10^2 \text{ MeV}$. This means that solar neutrinos, whose energy is $E_\nu \simeq 1 \text{ MeV}$ (as seen in figure 5.6) fall precisely in the resonance domain and, therefore, are subject to large flavor transitions that lead to the deficit in the flux measurement since CC interaction allows just for ν_e detection.

6

The Model

6.1 Modeling the Earth

In order to model the Earth, different assumptions were made. The most important one is, probably, that the Earth is azimuthally symmetrical, nevertheless the model to be shown will allow for some complex radial and polar asymmetries.

All programs developed for the project are available in the repository ¹ dedicated to it. Implementation is mainly done in C++, but a small part involving the probability calculations is done in Python.

For integrating, I use cylindrical coordinates, in which the z coordinate is, as usual $z \in [-R, R]$, where $R = 6371\text{km}$ is Earth's Radius. The radial coordinate is called $x \in [0, \sqrt{R^2 - z^2}]$. Thus, we divide the Earth in rings, or nodes (illustrated in fig. 6.1). Each ring will have a volume $dV = 2\pi x dx dz$ (figure 6.2b). Computationally, the Earth is modeled by a 500×1000 matrix of instances of the class `RingNode`, this type of data has a variety of attributes that will be introduced when necessary in this text.

¹https://github.com/dforero0896/Physics_Monograph

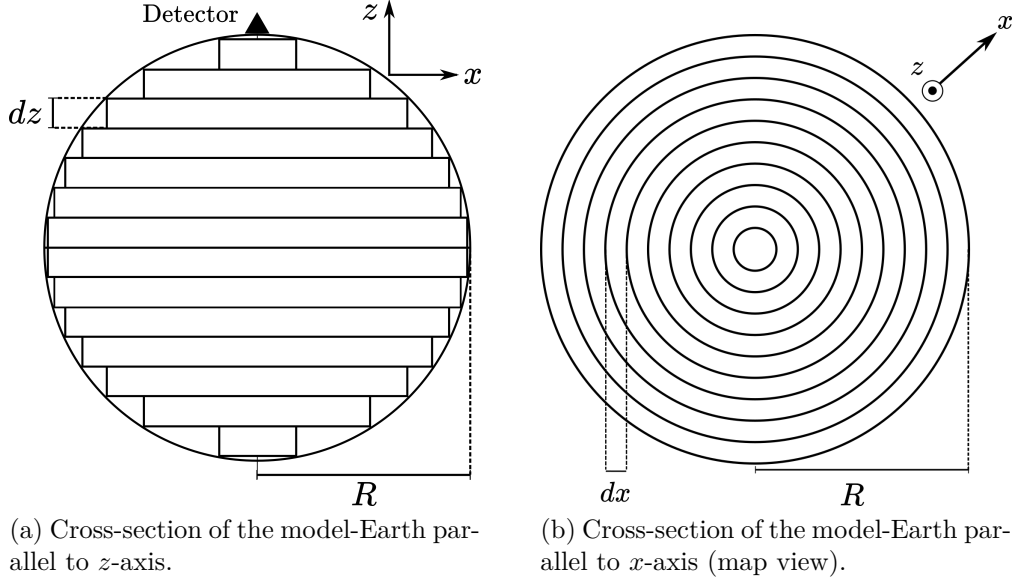


Figure 6.1: Diagram showing the discretization of the Earth and coordinates used. (a): Earth divided in discs perpendicular to z -axis of constant height dz . Each disc will be divided into rings as shown in (b), the number of rings is variable from disc to disc since dx is constant.

The matrix itself is an attribute of the class `Planet`, that holds other attributes such as total mass, volume and fluxes. Figure 6.2 shows different attributes of `RingNode` class. These classes are defined in `earth_simul.h` and the respective implementation file `earth_simul.cpp`.

6.2 Modeling the Flux

6.2.1 The Flux Integral

As in reference [21], the flux is given by the integral of equation 6.1.

$$\Phi_X(\mathbf{r}) = \frac{n_X \lambda_X}{4\pi} \int_{\Omega} \int_{\oplus} \frac{a_X(\mathbf{r}') \rho(\mathbf{r}') P_{ee}(\mathbf{r} - \mathbf{r}', E_\nu)}{|\mathbf{r} - \mathbf{r}'|^2} d^3 r dE_\nu \quad (6.1)$$

Here, n_X stands for the number of neutrinos produced in decay chain X (from equations 4.7 through 4.11), λ_X is the decay constant for each chain, a_X is the isotopic abundance at position \mathbf{r}' , defined as $a_X = \frac{A_X X_X}{M_X}$, where

| | ^{238}U | ^{232}Th |
|----------------------------|-----------|------------|
| X | 0.9927 | 1 |
| M (u) | 238.051 | 232.038 |
| $\tau_{1/2}$ | 4.468 | 14.05 |
| λ ($10^{-18}/s$) | 4.916 | 1.563 |
| n | 6 | 4 |

Table 6.1: Values of the different constants in equation 6.1. Taken from reference [21].

A is as defined in chapter 3, X_X is the isotopic ratio and M_X is the atomic mass. Then, ρ is the matter density and P_{ee} is the survival probability of the geoneutrinos produced at \mathbf{r}' with energy E_ν , travelling towards \mathbf{r} . Finally, the factor $\frac{1}{4\pi|\mathbf{r}-\mathbf{r}'|^2}$ accounts for the spherically divergent flux. The values used for these factors are shown in table 6.1. Integration should be done in domains \oplus (Earth) spatially and Ω , shown in figure 4.4, for the energy. All these quantities are attributes to the class `RingNode`.

6.2.2 Survival Probability

The quantity P_{ee} depends on both the path ($|\mathbf{r} - \mathbf{r}'|$) the geoneutrino takes, and the energy (E_ν) with which it is produced. The energy of these antineutrinos depends on the spectra ($\frac{dn}{dE_\nu}$) in figure 4.4. Given this dependency, we should, actually, calculate the following integral over energies:

$$\int_{\Omega} P_{ee}(\mathbf{r} - \mathbf{r}', E_\nu) \frac{dn_X}{dE_\nu} dE_\nu \quad (6.2)$$

We should be careful, because for the spectra $\frac{dn_X}{dE_\nu}$ in figure 4.4, $\int_{\Omega} \frac{dn_X}{dE_\nu} dE_\nu = n_X$; since we have already included the factor n_X in equation 6.1, the spectra in equation 6.2 should instead be normalized, such that $\int_{\Omega} \frac{dn'_X}{dE'_\nu} dE'_\nu = 1$, for this, we must perform the following calculation

$$\frac{dn'_X}{dE'_\nu} = \frac{\frac{dn_X}{dE_\nu}}{\int_{\Omega} \frac{dn_X}{dE'_\nu} dE'_\nu} \quad (6.3)$$

Upon discretization of the integral in equation 6.2, taking into account the normalization of the spectra, we get

$$\sum_i P_{ee}(\mathbf{r} - \mathbf{r}', E_{\nu,i}) w_i = \sum_i P_{ee}(\mathbf{r} - \mathbf{r}', E_{\nu,i}) \frac{f_i}{\sum_j f_j \Delta E_\nu} \Delta E_\nu. \quad (6.4)$$

Here, we have defined

$$f_i \equiv \left(\frac{dn_X}{dE_\nu} \right)_i = \frac{dn_X}{dE_\nu}(E_{\nu,i}), \text{ thus, } w_i = \frac{f_i}{\sum_j f_j}. \quad (6.5)$$

Taking into account these expressions, the way of performing the integral over the energies is the following: for a given node in the matrix, the path to the detector is calculated, for this path and $M = 100$ samples of energy ($E_{\nu,i}$), the survival probability ($P_i \equiv P_{ee}(\mathbf{r} - \mathbf{r}', E_{\nu,i})$) is obtained. Then, for the same energies, the spectra is sampled, this results in M values f_i . Each is normalized as $w_i = f_i / \sum_j f_j$. These w_i are the weights corresponding to each probability. Finally the probability for each node is

$$P_{ee}(|\mathbf{r} - \mathbf{r}'|) = \sum_i w_i P_i. \quad (6.6)$$

There are three programs that handle this step: `raw_probs.cpp` that calculates the raw probabilities (as previously mentioned in section 5.3.2) for a node and writes them in the file `raw_probs.csv`, `prob_weight.cpp` that calculates the weights w_i for a node and exports them to a file `prob_weight.dat` and `prob_integrating.py` that is in charge of running the C++ programs for all node i, j in the Earth and calculating the “average” probability for each one (equation 6.6) and writing them to file `probability_planet.csv`, which is used in the calculations of the flux.

It is worth mentioning that prior studies use an average probability given by approximating the two-flavor oscillation model (equation 5.46).

6.3 Terrestrial Neutrino Units

Terrestrial Neutrino Units (TNU) is the usual unit used in (anti)neutrino experiments. TNU is defined as the number of interactions in one year

when using a target of 10^{32} protons and 100% detection efficiency. Reference [13] defines the conversion as follows, where $S(X)$ is in TNU and Φ_X is in $cm^{-2}/\mu s$.

$$S(^{232}Th) = 4.07\Phi_{Th} \quad (6.7)$$

$$S(^{238}U) = 12.8\Phi_U \quad (6.8)$$

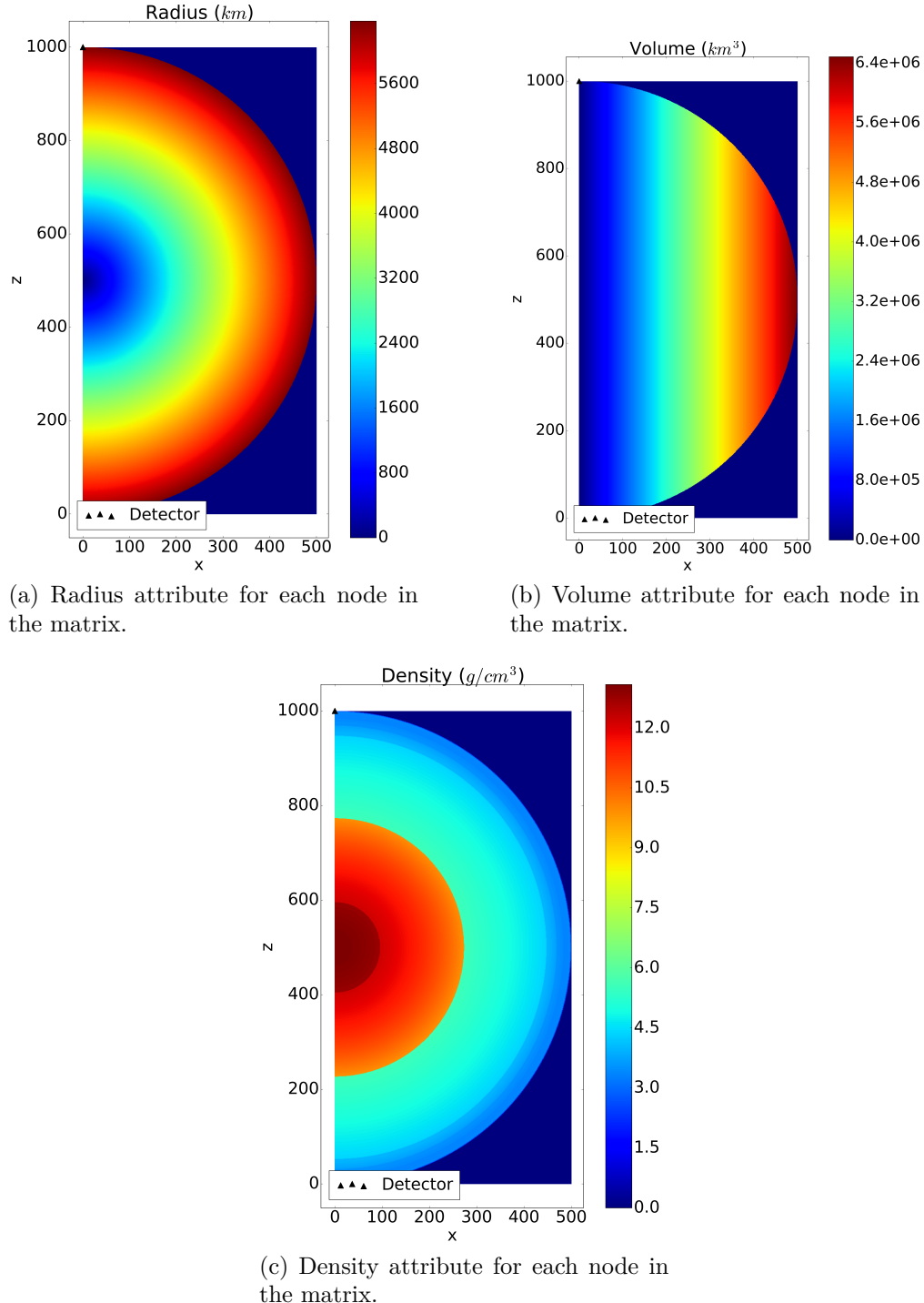


Figure 6.2: Various plots showing different attributes of class `RingNode`.
 (a): Radius for each node in the matrix. (b): Volume for each node.
 (c): Density of each node according to the PREM model [5]. The radial coordinate (x-axis) is labeled x and the z coordinate is labeled z .

7

UANdINO

As stated before, UANdINO is a C++, GSL-based program that, given a density path and an (anti)neutrino energy, calculates the survival probability. It is entirely based on the work done in reference [16]. The development of this software was a crucial part of this work and the idea is that everybody, who needs it, is able to use it. Its source code consists of a header file `uandino.h` and an implementation file `uandino.cpp`.

7.1 Path generation and number of steps

Given the structure of the program that simulates the Earth which includes an attribute `path` to each object of the class `RingNode`, UANdINO must be given a “path” parameter. The generation of this paths must, therefore, be done before calling the `calculateProbabilities` function from UANdINO. This takes a lot of time, mainly because of the huge amount of elements to be allocated (the same number of spatial steps to be made, $\sim 10^6$). Because of this, the paths must be stored in dynamically-allocated structures, such as dynamically-allocated arrays or, in this case, C++ `vector<double>` structures. These must be stored in the heap (as opposed to the stack) and it takes more time to do so, too. Nevertheless, a slight modification in UANdINO’s source code will allow it to work on a given density function (not a density array). This will greatly improve performance but is of no practical use in this particular project, given that the functions change from node to node in the matrix.

The huge amount of spatial steps mentioned earlier is a consequence of an extreme *sensibility* from UANdINO, regarding the length of each step (L , from equation 5.46). This *sensibility* means that the program works better with a really small step ($\sim 10^{-4}$ km) and still, at low energies it ceases to work. In the region of $E_\nu < 10^5$ eV, the probability overflows. The obvious, though foolish, solution would be to increase the number of steps. This would, clearly, increase the time taken by the program for the allocation of the path in memory, which would sooner or later run out, and in the calculation of the probability itself. The relation between time and number of steps is shown in figure 7.1.

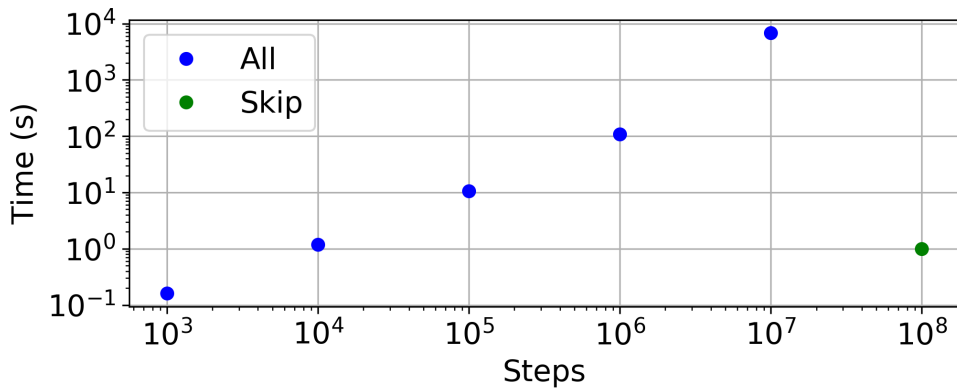


Figure 7.1: Time taken by UANDINO to calculate the survival probability of a neutrino produced in the center of the Sun. Blue dots indicate the time taken when the evolution operator is calculated for each iteration. Green dot shows the case in which some iterations are skipped.

7.2 Optimization in steps: Skipping

No matter how “rapidly” the density function, or array, is changing, it won’t change at all in between steps this small, which means that 10^6 steps is an overkill. We could, and should, use much bigger steps; this way, there would be less iterations, but the results would be compromised at low energies. The workaround the latter is given by “skipping” some

iterations. For instance, the Earth’s density will be correctly sampled with “big” steps of $L_b \sim 10 \text{ km}$. If we choose a “small” step length of $L_s \sim 10^{-4} \text{ km}$, as to make sure that the method works at relatively low energies, we could establish that

$$U(L_b) = \exp(iHL_b) = \exp(iH(nL_s)) = \exp(iHL_s)^n = U(L_s)^n. \quad (7.1)$$

Thus, we would be able to calculate the time-evolution operator $U(L_s)$ and then exponentiate it. Therefore, instead of n iterations calculating n times the same operator $U(L_s)$, we would have $\log_2(n) \ll n^1$, for example, in the case in which we skip $n \sim 10^5$ iterations, we would be able to replace them with $i_{\max} \sim 17$, leading to a significant reduction in the time, also shown in figure 7.1 by the green dot.

7.3 Parallelization

UANDINO’s main two functions, calculate the time-evolution operator and the probabilities. The latter uses nested loops: for each one of the M energies to consider, the program calculates the operator for each one of the steps in distance (path). The outer, energy, loop stores the different probabilities in an array, previously allocated in the stack. This implementation, allows a rather easy parallelization using OpenMP. On the other hand, the inner, path loop, is not parallelized due to the potential problems this may generate, for instance, the product of time-evolution operators should be time-ordered, and there’s no way for us to be sure that the different cores will finish the calculations just in time for this to happen.

Regarding the HPCC, most of the testing, and final calculations, were done with 3 or 4 nodes with 32 cores each. So, if calculating, for example, 100 energies, the 3-node approach will have 96 cores, 92 of them will calculate the probabilities for one energy while, probably, 4 of them will calculate 2 energies.

¹The first iteration will be $U(L_s)U(L_s) = U(L_s)^2$, the second will be $U(L_s)^2U(L_s)^2 = U(L_s)^4$ and the i -th will, therefore, yield $U(L_s)^{2^i}$, so the maximum number of iterations will be $i_{\max} = \log_2 n$.

7.4 Accuracy tests

7.4.1 Two-flavor neutrinos

In order to test the functionality of the software, I reproduced some plots of said reference, check Appendix A.

The effective potential used in most of the graphs is $\mathcal{A} = 10^{-13}$ eV, according to the MSW effect we should expect resonances as $E_\nu \rightarrow 10^{10}$ due to the $\Delta m^2 \sim 10^{-5}$ used by the authors in reference [16]. Figures A.1 through A.13 show accurately the effect.

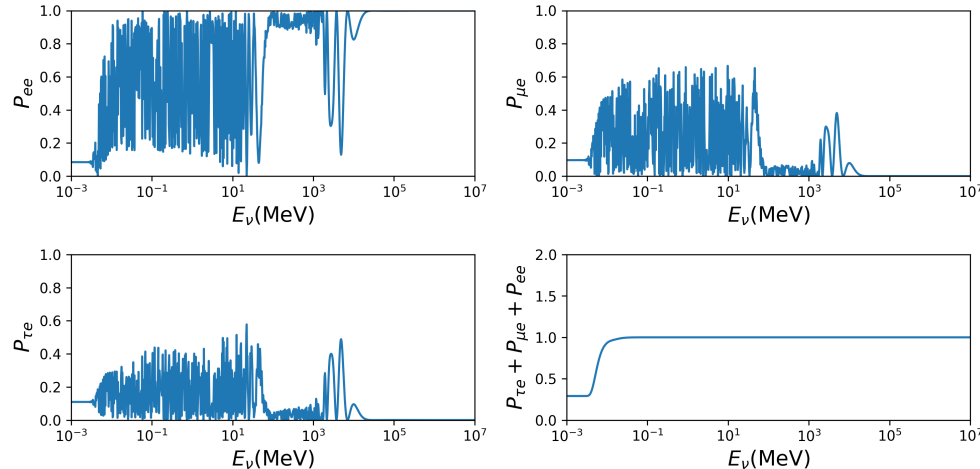


Figure 7.2: Neutrino probabilities for a step-function potential from figure 1 of reference [16] and real oscillation parameters from reference [17].

Figure 7.2 shows the transition and survival probabilities for neutrinos propagation through the potential of figure 1 from reference [16]. Note that the resonances lay around the MSW-predicted values. The frequency of the oscillation also increases significantly at lower energies, as expected. Also, note that at these energies, the program starts failing as shown by the lower-right plot in figure 7.2. This could be solved by a smaller step length, but even with skipping, it would, unnecessarily, increase the time taken by the program.

7.4.2 Solar Neutrinos

Solar neutrinos and the so-called *Solar Neutrino Problem* were key issues in the physics research of the last decade. Different authors (references [4, 20], for example) published experimental results on the survival probability of electron neutrinos produced in the Sun. Nowadays, it is widely believed that enough has been said in this area and some reviews, such as reference [23] have emerged. This is to say that solar neutrino oscillations is a widely studied topic and therefore, a good way to certify that UAndINO gives appropriate results.

Figure 7.3 shows the average solar neutrino survival probability as reported in various references ([4, 17, 20, 23]) alongside the result of the UAndINO simulation for the sun. Notice that in all cases, at low energies $P_{ee} \rightarrow 0.6$, while at the higher boundary $P_{ee} \rightarrow 0.35$. Evidently, the simulation is in agreement with the averaged measurements presented. Additionally, an average survival probability $P_{ee} \approx 0.35$ solves the Solar Neutrino Problem, as expected [1].

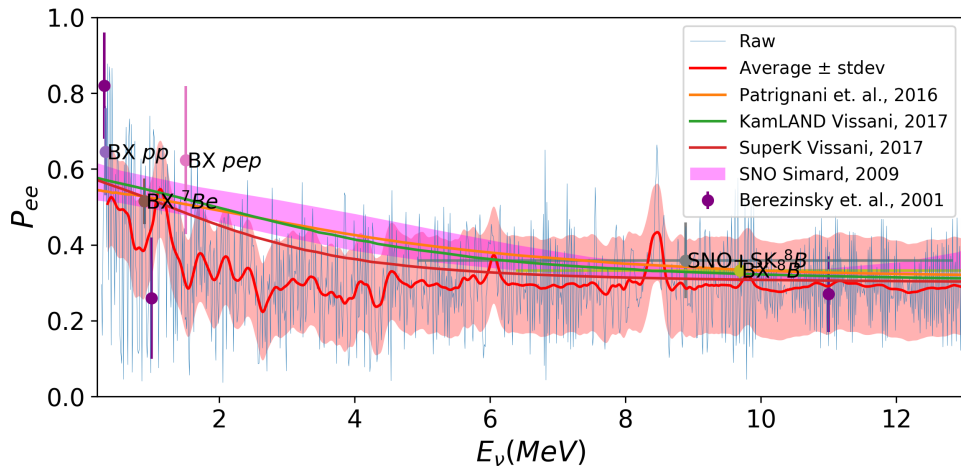


Figure 7.3: Survival probability for solar ν_e as given by different experiments/publications. Dots are measurements from Borexino (BX) and SNO + Super Kamiokande (SK) reported in reference [17] as well as those from reference [4].

8

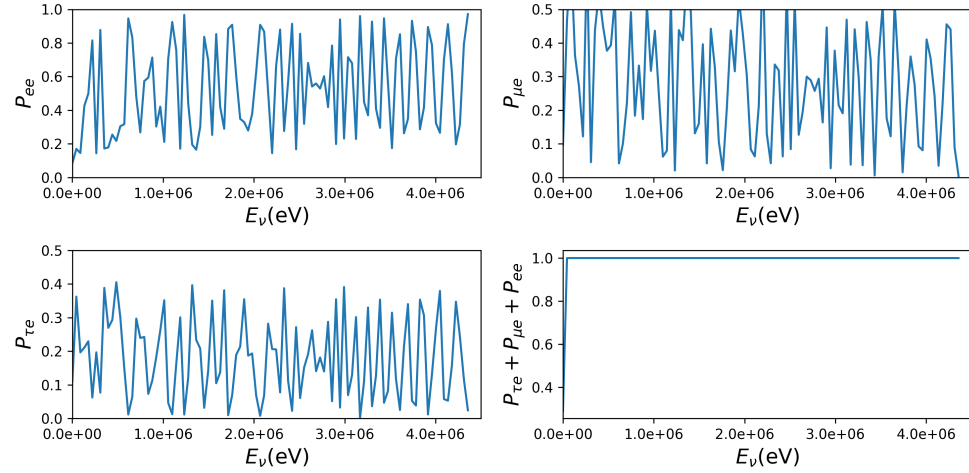
Results

8.1 UANdINO

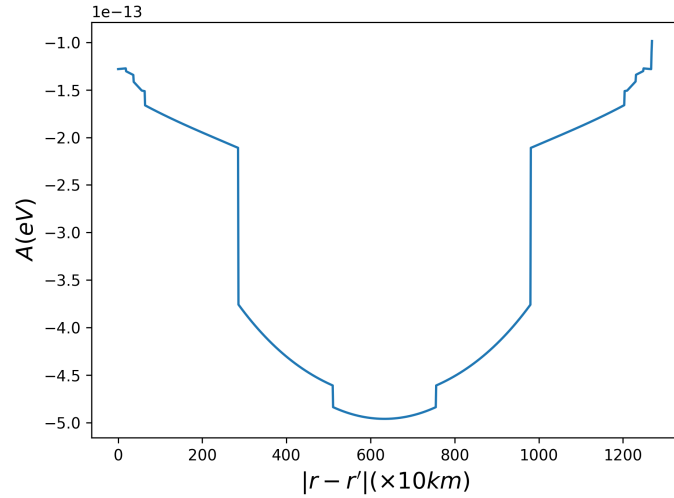
The UANdINO run was programmed in a Python script that called it iteratively for each path and all energies. This was done for all different combinations of HPE distributions and BSE models. This run was made in the HPCC of the university and took about $150\ h = 6.5\ d$ for each BSE.

Figure 8.1a shows the antineutrino survival probability for such a particle crossing the potential shown in figure 8.1b. At first glance, it is evident that, different from figure 7.2, there are no resonances. This should be clear from equation 5.39 too, given that in the case of antineutrinos $\mathcal{A} < 0$, the condition is not met. Antineutrinos are not subject to the MSW effect. Nevertheless, they still fill some potential that affects P_{ee} . Appendix B shows plots for different paths inside the Earth to show the dependence of the probability on these. Figure 8.2 shows the energy-integrated survival probabilities for each node in the Earth obtained by UANdINO.

The probabilities obtained from the software are such that the equiprobable regions form concentric circles centered in the detector. The mean, minimum and maximum values obtained from the simulation are $\langle P_{ee} \rangle = 0.56154$, $P_{ee}^{min} = 0.2$ and $P_{ee}^{max} = 0.92$ for figure 8.2a; and $\langle P_{ee} \rangle = 0.56026$, $P_{ee}^{min} = 0.34$ and $P_{ee}^{max} = 0.78$ for figure 8.2b. Notice that the probability in the latter oscillates with a much higher frequency. In any case, the mean values are close to the vacuum value of $\langle P_{ee} \rangle_{vac} = 0.56$ shown in figure 5.4. Apparently, in the case of geoneutrinos, the survival probability



(a) Survival and transition probabilities given by UAndINO for 100 energies in the relevant domain, Ω .



(b) Potential A felt by geoneutrinos crossing, diametrically, the Earth.

Figure 8.1: P_{ee} and path from node (1, 1) (diameter).

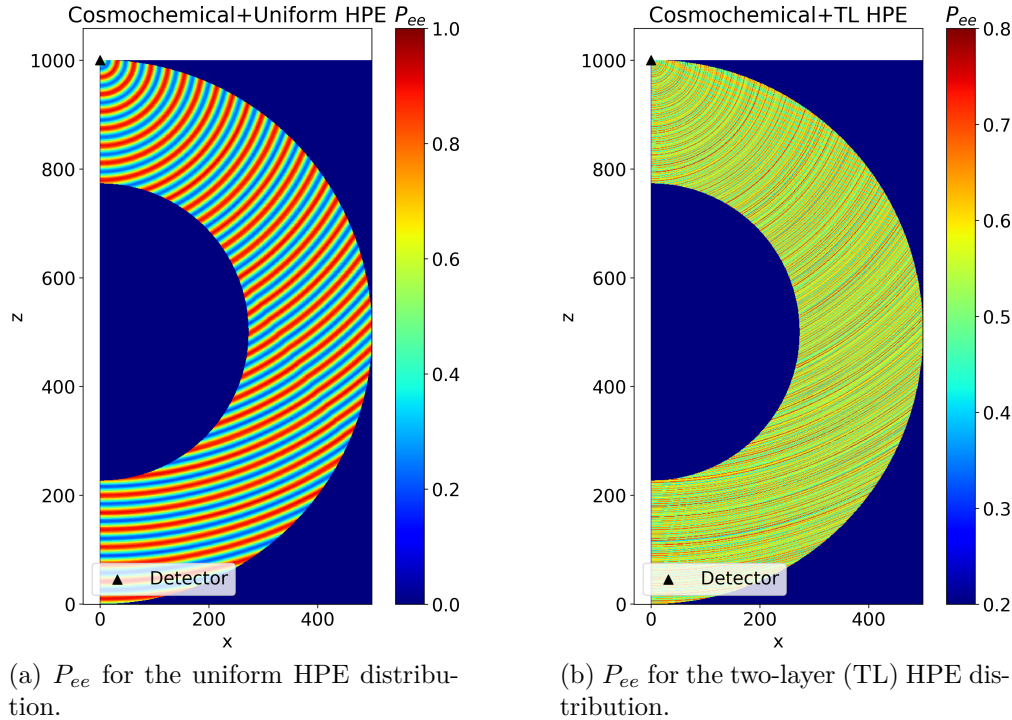


Figure 8.2: Energy-integrated P_{ee} for each path (node) in the Earth, from UANdINO. Even though only cosmochemical BSE is shown, all other BSE's give almost the same result.

is not greatly affected by the presence of matter, but mainly depends, on the distance to the detector.

8.2 Flux simulation

Following the work in reference [21], a test with an average survival probability (from reference [13]) of $\langle P_{ee} \rangle_{app} = 0.55$ from the two-flavor approximation, the different HPE distributions and BSE models was done, the results are shown in table 8.1. On the other hand, table 8.2 shows the results when using UANdINO's probabilities.

The simulation allows for an inspection on the distribution of the flux. Figure 8.3 shows the flux contribution to the total for both isotopes in the two-layer HPE distribution model. Figure 8.4 shows them for the uniform

| BSE Model \HPE distribution | Uniform | | Two-layer | |
|-----------------------------|----------|-------------|-----------|-------------|
| | Φ_U | Φ_{Th} | Φ_U | Φ_{Th} |
| Geochemical | 0.626 | 0.526 | 0.530 | 0.436 |
| Cosmochemical | 0.242 | 0.139 | 0.236 | 0.140 |
| Geodynamical | 1.345 | 1.158 | 1.079 | 0.917 |

Table 8.1: First results on geoneutrino flux from the mantle (in $cm^{-2}/\mu s$) for different BSE and HPE distribution models. Using average probability from two-flavor approximation.

| BSE Model \HPE distribution | Uniform | | Two-layer | |
|-----------------------------|----------|-------------|-----------|-------------|
| | Φ_U | Φ_{Th} | Φ_U | Φ_{Th} |
| Geochemical | 1.123 | 0.947 | 0.949254 | 0.781 |
| Cosmochemical | 0.435 | 0.250 | 0.426233 | 0.251 |
| Geodynamical | 2.414 | 2.078 | 1.930 | 1.640 |

Table 8.2: Results on geoneutrino flux from the mantle (in $cm^{-2}/\mu s$) for different BSE and HPE distribution models. Using UAndINO probability.

HPE.

One should note that, even though abundance of thorium is higher in every layer, its contribution to the total flux seems to be lower and less spatially spread. This can be attributed to the number of antineutrinos per chain, n_X : ^{238}U produces 2 antineutrinos more in each decay, compared to ^{232}Th . This holds for the other BSE models

For the whole silicate Earth and average probability the flux is shown in table 8.3. When using the probabilities given by UAndINO for each node the results are quite different. These are shown in table 8.4.

| BSE Model \HPE distribution | Uniform | | | Two-layer | | |
|-----------------------------|---------|----------|-----------|-----------|----------|-----------|
| | S_U | S_{Th} | S_{tot} | S_U | S_{Th} | S_{tot} |
| Geochemical | 5.357 | 15.046 | 20.403 | 4.968 | 13.876 | 18.844 |
| Cosmochemical | 3.797 | 10.074 | 13.870 | 3.777 | 10.081 | 13.858 |
| Geodynamical | 8.283 | 23.110 | 31.393 | 7.202 | 20.031 | 27.233 |

Table 8.3: Whole SE results on geoneutrino flux (TNU) for different BSE and HPE distribution models, using two-flavor approximation for survival probabilities.

| BSE Model \HPE distribution | Uniform | | | Two-layer | | |
|-----------------------------|---------|----------|-----------|-----------|----------|-----------|
| | S_U | S_{Th} | S_{tot} | S_U | S_{Th} | S_{tot} |
| Geochemical | 9.617 | 27.010 | 36.627 | 8.909 | 24.881 | 33.79 |
| Cosmochemical | 6.816 | 18.086 | 24.902 | 6.780 | 18.098 | 24.879 |
| Geodynamical | 14.869 | 41.481 | 56.350 | 12.900 | 35.881 | 48.781 |

Table 8.4: Whole SE results on geoneutrino flux (TNU) for different BSE and HPE distribution models, using UAndINO’s results for survival probabilities.

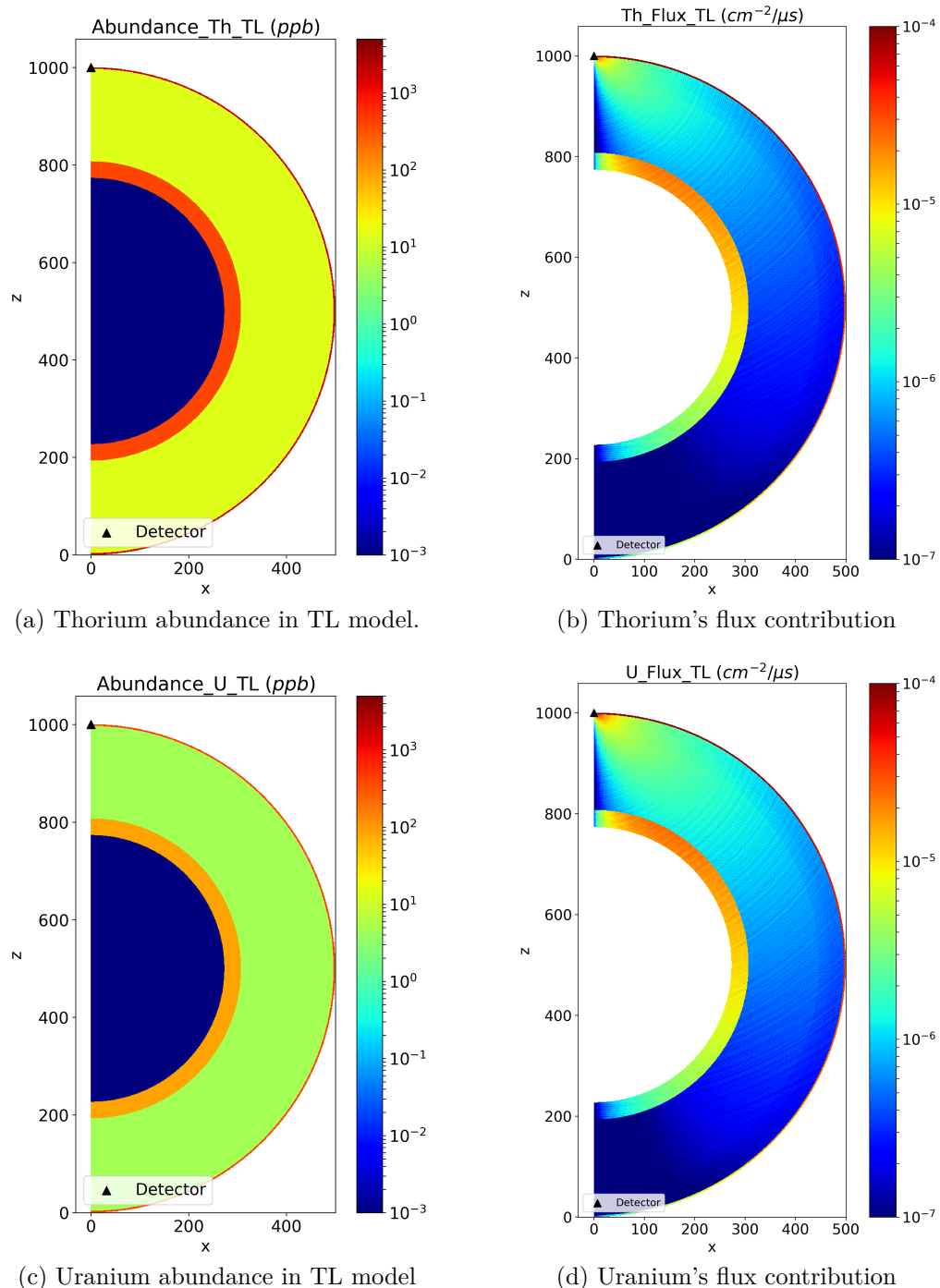


Figure 8.3: HPE abundance model (left) and flux contribution (right) for U (a,b) and Th (c, d) in the two-layer HPE distribution model. Example with geochemical BSE.

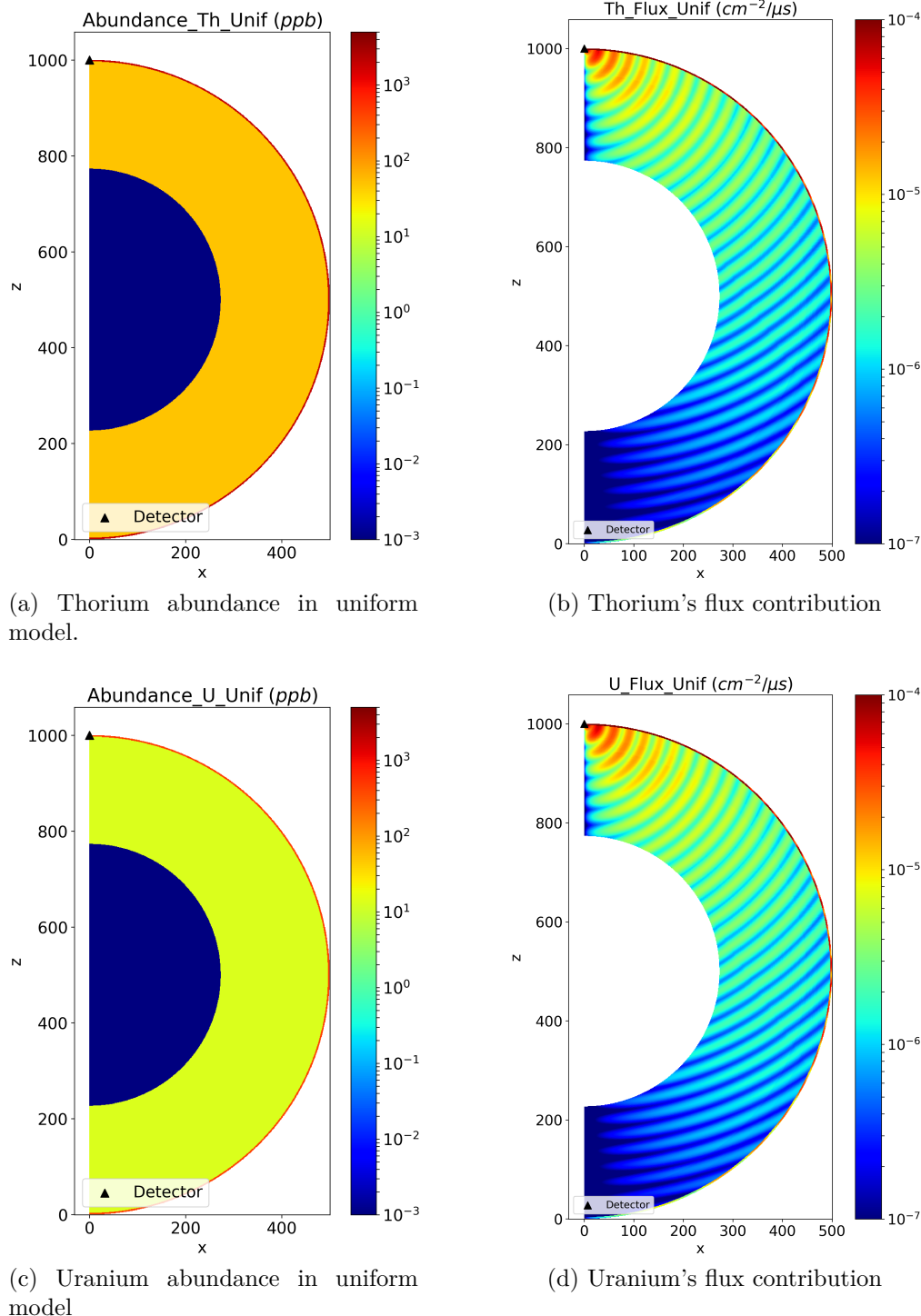


Figure 8.4: HPE abundance model (left) and flux contribution (right) for U (a,b) and Th (c, d) in the two-layer HPE distribution model. Example with geochemical BSE.

9

Analysis

The results previously shown are to be analyzed in two ways, the mantle-only and whole Earth fluxes through comparison with real data taken by KamLAND and Borexino geoneutrino experiments which are located in Japan and Italy, respectively. According to reference [13], the measured flux values are those shown in table 9.1.

| | Borexino | KamLAND |
|-----------------------------|---------------|---------------|
| $S_{tot}(TNU)$ | 38.8 ± 12 | 30 ± 7 |
| $\Phi_{tot}(cm^{-2}/\mu s)$ | 4.4 ± 1.4 | 3.4 ± 0.8 |

Table 9.1: Experimental values for geoneutrino flux in detectors Borexino and KamLAND. Taken from reference [13].

In the first place, figure 9.1 the mantle fluxes from U and Th using UANdINO's probability and the two-flavor oscillation approximation one (recall, $\langle P_{ee} \rangle = 0.55$) are shown, in comparison to reference [21], in which the integral 6.1 is used too. For both isotopes, even though the simulation is close to the values given in said reference, they are not within the uncertainties there given.

On the other hand, UANdINO shows values that are, in the case of geochemical and geodynamical BSE models, way higher than expected, but the cosmochemical BSE model values are actually closer to those expected from reference [21] than the ones calculated with the two-flavor approximation. Then, the addition of both contribution yields the total

values for the mantle expected signal in TNU are shown in figure 9.1c. In reference [13] a combined analysis of the results in table 9.1 is done, which results in a central value for the mantle signal of $7.7 \pm 6.2 TNU$. Taking this into account, UANdINO shows results outside of the expected range in 2/3 BSE models, confirming what we said before regarding the accuracy of its results in this case.

In the second place, figure 9.2 shows the results of both simulations (UANdINO's and two-flavor probabilities) along with the measurements of the detectors according to [13]. In this case, the UANdINO results look promising since they are within the expected range in 2/3 BSE models. The results show that the geochemical BSE model fits best to the available data as seen in figure 9.2. Additionally in figure 9.1c, the closest value from UANdINO's simulation is also the geochemical BSE model. These, rather small, discrepancies can be attributed to the uncertainties in the integration of the flux, product of the discretization of the Earth. If we looked only at the two-flavor approximation, the best-fitting one is still the geochemical, since it is closer to the central value of $7.7 TNU$.

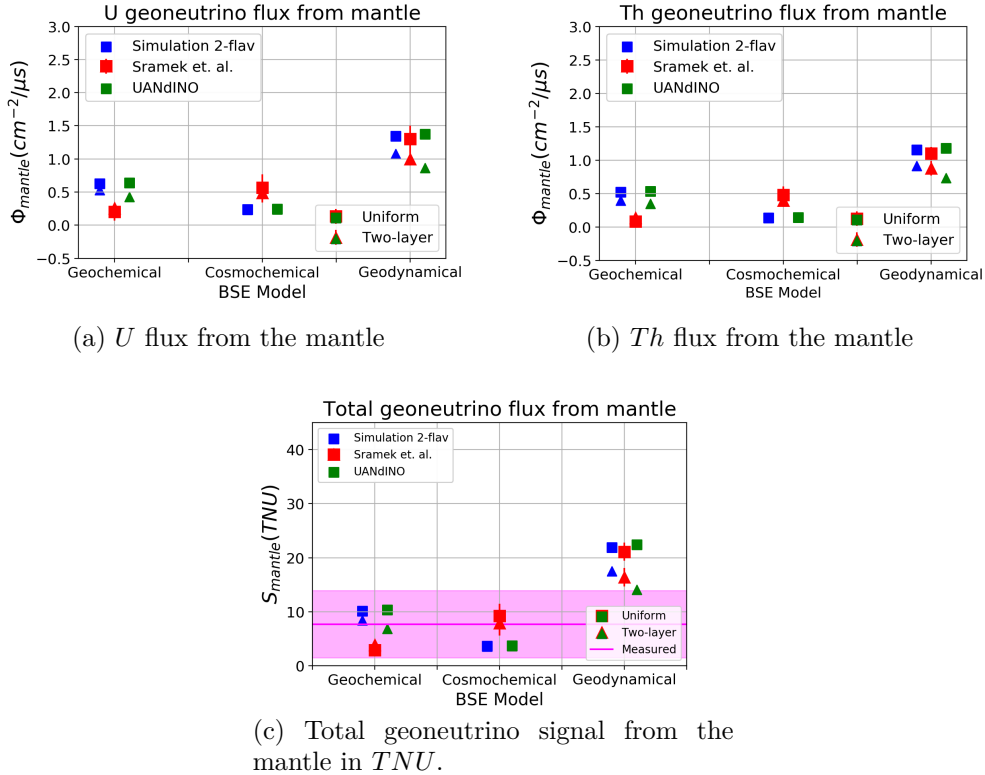


Figure 9.1: (a): Mantle fluxes due to U in different cases: both simulations and data from [21]. (b): Mantle flux due to Th , analogous data to that of U . Note that in this case, the two.flavor approximation results (blue) are closer to those from the literature (red) than the UANDINO simulation (green). In general, the two-layer model (triangles) results in lower values for the flux. (c): Geoneutrino signal expected from the mantle for the different models and the expected signal from detectors according to reference [13].

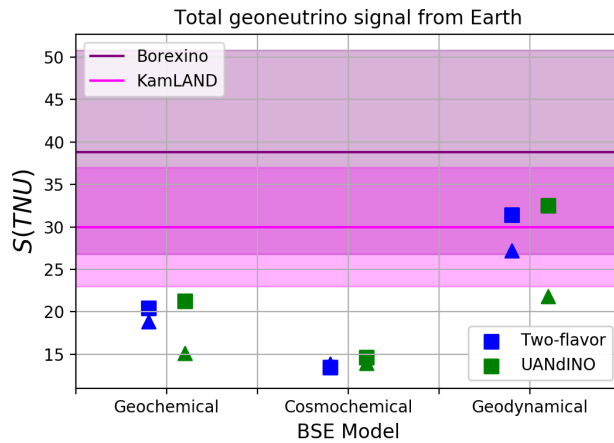


Figure 9.2: Total geoneutrino flux expected from the different models. Triangles are still two-layer and squares, uniform HPE distributions. Colored bands correspond to signals measured by the detectors according to reference [13]. In this case, UANDINO's probability results show a better agreement to the experimental data, specially geochemical BSE model.

10

Conclusions

The main goal for this work was to discriminate between the different HPE distribution models by using rigorous neutrino matter oscillation formalism, since this has been a debate in geoscience given the multiple models for the mantle that rely on information such as it's dynamics or heat flow product of radioactive decay. The introduction of new information coming from neutrino geoscience may be the necessary step to link the available information and draw conclusions.

First, one should look at which of the BSE models shows a better fit with the data available from the detectors. In this matter, the geochemical BSE model is the one, since in the total expected flux of figure 9.2 it seems to be an average between Borexino and KamLAND measurements. This is important since these detectors are in radically different geological settings, which is said to affect the geoneutrino flux; while the simulation is in “average” Earth. In the case of the mantle expected flux (fig. 9.1c), the geochemical BSE model is also the one closer to the central value and to the expected area. The discrepancies can be attributed to uncertainties in the integration, mainly given by the discretization of the planet.

Then, regarding the HPE distributions, we can conclude that, even though the two models give rather similar results, the ones of the two-layer model can be closer to the measured values, nevertheless, the results are not entirely conclusive in this respect.

10.1 Further Directions

As I stated before, geoneutrinos are a rather new tool in geophysics and Neutrino Geoscience a new field in geoscience, there is a lot more work to do and problems to solve.

Further work is needed, especially regarding the difference between the survival probability given by the software and the average one given in the literature, and why, despite these quite different probabilities, the results in terms of geoneutrino flux are still reasonable. This involves additional testing to UAndINO to certify the accuracy of the results.

On the other hand, the Earth modeling was satisfactory, since it allowed to reproduce some of the basic properties of the planet and gave some liberties on parameters such as the HPE abundances and their distribution. Nevertheless, the mantle is known to be way more complex than the two-layer model. This model can be refined in order to include mantle heterogeneities result of convection that leads to subducting crust, thus, increasing HPE abundance in the mantle. Unfortunately, these modifications are not trivial and a big part of the software might have to be rewritten.

References

- [1] Michael F Altmann, Rudolf L MöSSbauer, and Lothar J N Oberauer. “Solar neutrinos”. In: *Reports on Progress in Physics* 64.1 (Jan. 2001), pp. 97–146. ISSN: 0034-4885. DOI: 10.1088/0034-4885/64/1/203. URL: <http://stacks.iop.org/0034-4885/64/i=1/a=203?key=crossref.f5e6ab9425ef6027dd8df16f37c931f5>.
- [2] John N. Bahcall. “Solar Models and Solar Neutrinos: Current Status”. In: (Dec. 2004). DOI: 10.1088/0031-8949/2005/T121/006. arXiv: 0412068 [hep-ph]. URL: <http://arxiv.org/abs/hep-ph/0412068%20http://dx.doi.org/10.1088/0031-8949/2005/T121/006>.
- [3] John N Bahcall and Carlos Peña-Garay. “Solar models and solar neutrino oscillations”. In: *New Journal of Physics* 6 (2004). DOI: 10.1088/1367-2630/6/1/063. URL: <http://www.njp.org/>.
- [4] V Berezinsky and M Lissia. “Electron-neutrino survival probability from solar-neutrino data”. In: *Physics Letters B* 521.3-4 (Nov. 2001), pp. 287–290. ISSN: 0370-2693. DOI: 10.1016/S0370-2693(01)01212-6. URL: <https://www.sciencedirect.com/science/article/pii/S0370269301012126>.
- [5] Adam M. Dziewonski and Don L. Anderson. “Preliminary reference Earth model”. In: *Physics of the Earth and Planetary Interiors* 25.4 (1981), pp. 297–356. ISSN: 00319201. DOI: 10.1016/0031-9201(81)90046-7.
- [6] S Eidelman et al. “Review of Particle Physics”. In: *Physics Letters B* 592 (2004), pp. 1+. URL: <http://pdg.lbl.gov>.

- [7] S. Enomoto. “Neutrino Geophysics and Observation of Geo-Neutrinos at KamLAND”. Doctoral Dissertation. Tohoku University, 2005. URL: <http://kamland.stanford.edu/GeoNeutrinos/GeoNuResult/SanshirosDoctoralDissertation.pdf>.
- [8] Mark Galassi et al. *GNU Scientific Library Release 2.4*. 2017. URL: <https://www.gnu.org/software/gsl/doc/latex/gsl-ref.pdf>.
- [9] Carlo Giunti and Chung W. Kim. *Fundamentals of Neutrino Physics and Astrophysics*. 1st ed. New York: Oxford University Press, Mar. 2007, pp. 1–728. ISBN: 9780198508717. DOI: 10.1093/acprof:oso/9780198508717.001.0001. URL: <http://www.oxfordscholarship.com/view/10.1093/acprof:oso/9780198508717.001.0001/acprof-9780198508717>.
- [10] Victor Goldschmidt. *Geochemistry*. 1st ed. The Clarendon Press, 1958.
- [11] Yu Huang et al. “A reference Earth model for the heat-producing elements and associated geoneutrino flux”. In: *Geochemistry, Geophysics, Geosystems* 14.6 (2013), pp. 2003–2029. ISSN: 15252027. DOI: 10.1002/ggge.20129. arXiv: 1301.0365.
- [12] Kenneth S. Krane. *Introductory Nuclear Physics*. Wiley, 1988. ISBN: 9780471805533. DOI: 9780471805533.
- [13] L. Ludhova and S. Zavatarelli. “Studying the earth with geoneutrinos”. In: *Advances in High Energy Physics* 2013 (2013). ISSN: 16877357. DOI: 10.1155/2013/425693. arXiv: 1310.3961.
- [14] Shen-Su McDonough, William F; Sun. “The Composition of The Earth”. In: *Chemical Geology* 120 (1995), pp. 223–253. ISSN: 00092541. DOI: 10.1016/0009-2541(94)00140-4.
- [15] Scott M. McLennan. “Relationships between the trace element composition of sedimentary rocks and upper continental crust”. In: *Geochemistry, Geophysics, Geosystems* 2.4 (Apr. 2001), n/a–n/a. ISSN: 15252027. DOI: 10.1029/2000GC000109. URL: <http://doi.wiley.com/10.1029/2000GC000109>.

- [16] Tommy Ohlsson and Hakan Snellman. “Neutrino oscillations with three flavors in matter of varying density”. In: *The European Physical Journal C* 20.3 (2001), pp. 507–515. ISSN: 1434-6044. DOI: 10.1007/s100520100687. arXiv: 0103252 [hep-ph]. URL: <https://arxiv.org/abs/hep-ph/0103252>.
- [17] C. Patrignani et al. “Review of particle physics”. In: *Chinese Physics C* 40.10 (2016). ISSN: 16741137. DOI: 10.1088/1674-1137/40/10/100001. arXiv: 0402007 [gr-qc].
- [18] R.L. Rudnick and S. Gao. “3.01 Composition of the Continental Crust”. In: *Treatise on Geochemistry*. 2003, pp. 1–64. ISBN: 9780080437514. DOI: 10.1016/B0-08-043751-6/03016-4. URL: <http://www.sciencedirect.com/science/article/pii/B0080437516030164>.
- [19] Juan Carlos Sanabria. *La Simetría SU(2)xU(1)*. Bogotá, 2012. URL: <https://fisindico.uniandes.edu.co/indico/materialDisplay.py?materialId=slides%7B%5C%7DconfId=26>.
- [20] Olivier Simard. “Measurement of the Survival Probability and Determination of the Three-Flavor Neutrino Oscillation Parameters at the Sudbury Neutrino Observatory”. Doctoral Dissertation. Carleton University, 2009. URL: <https://sno.phy.queensu.ca/papers/osimard%7B%5C%7Dphd%7B%5C%7Dthesis%7B%5C%7D2009.pdf>.
- [21] Ondrej Sramek et al. “Geophysical and geochemical constraints on geoneutrino fluxes from Earth’s mantle”. In: *Earth and Planetary Science Letters* 361 (2013), pp. 356–366. ISSN: 0012821X. DOI: 10.1016/j.epsl.2012.11.001. arXiv: <arXiv:1207.0853v2>.
- [22] Stuart Ross Taylor and Scott M. McLennan. “The geochemical evolution of the continental crust”. In: *Reviews of Geophysics* 33.2 (May 1995), p. 241. ISSN: 8755-1209. DOI: 10.1029/95RG00262. URL: <http://doi.wiley.com/10.1029/95RG00262>.
- [23] Francesco Vissani. “Solar neutrino physics on the beginning of 2017”. In: *Nuclear Physics and Atomic Energy* 18.1 (2017), pp. 5–12. ISSN: 20740565. arXiv: 1706.05435.
- [24] K Hans Wedepohl. “The composition of the continental crust”. In: *Geochimica et Cosmochimica Acta* 59.7 (Apr. 1995), pp. 1217–1232. ISSN: 00167037. DOI: 10.1016/0016-7037(95)00038-2. URL: <http://www.sciencedirect.com/science/article/pii/0016703795000382>.

Appendices

Appendix A

Graph reproduction

In reference [16], besides the method, some graphs regarding the transition and survival probabilities of neutrinos passing through different density profiles, mostly step functions that aim at modeling the Earth. The oscillation parameters used are such that they correspond to a two-flavor case (table A.1), given that only 1 squared-mass-difference is different from zero. This is shown as a single resonance in the probabilities. One can also see that $P_{\tau e}$ and $P_{\mu e}$ are the same due to this reason.

In order to check my own implementation of the method, I reproduced these graphs, results are shown below.

Notice that figures A.12 and A.14 are not exactly the same as those obtained in said reference. The reason for this is that I did not actually understand which density profile they used.

| Parameter | Value |
|-----------------|---------------------------|
| Δm_{32} | $3.2 \times 10^{-3} eV^2$ |
| Δm_{21} | 0 |
| θ_{12} | 45° |
| θ_{23} | 45° |
| θ_{31} | 5° |

Table A.1: Two-flavor oscillation parameters from reference [16].

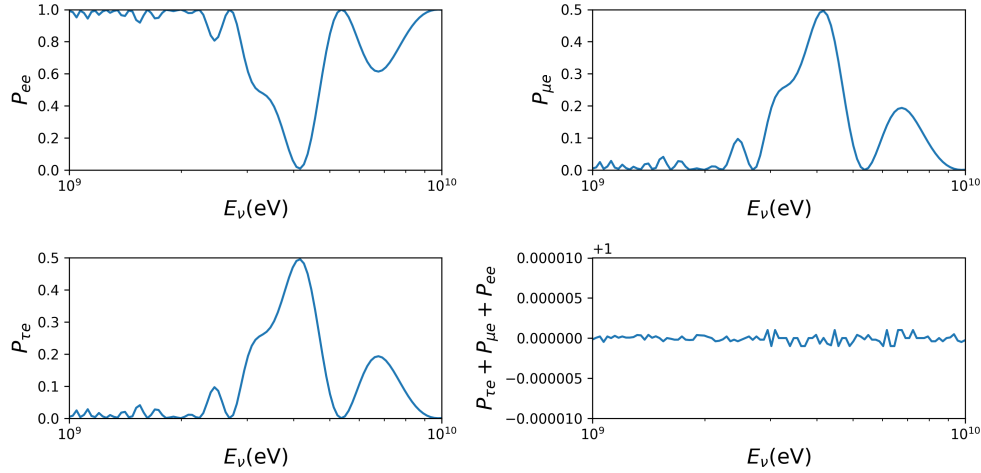


Figure A.1: UANdINO's result for figure 1 in reference [16].

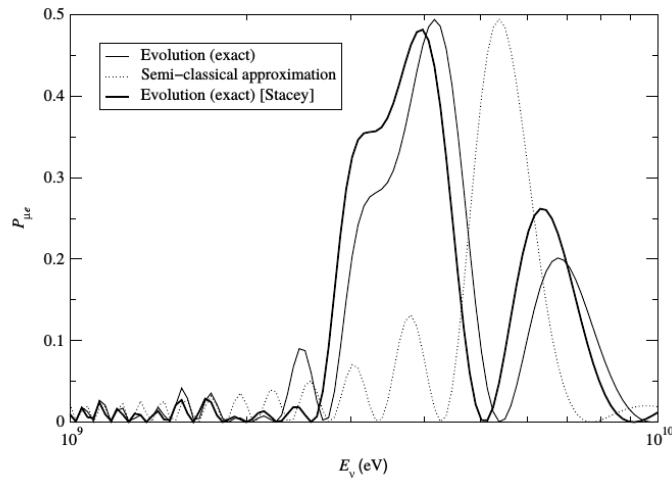


Figure A.2: Figure 1 taken from reference [16].

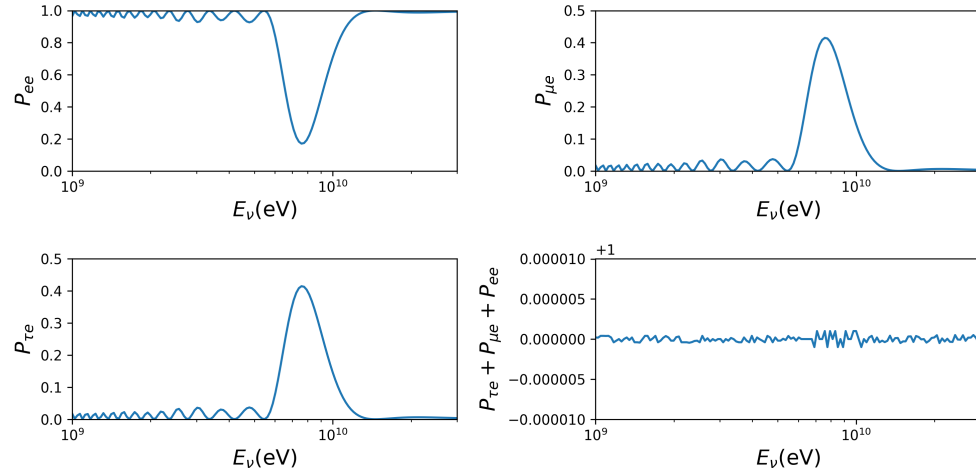


Figure A.3: UANdINO's result for figure 2 in reference [16].

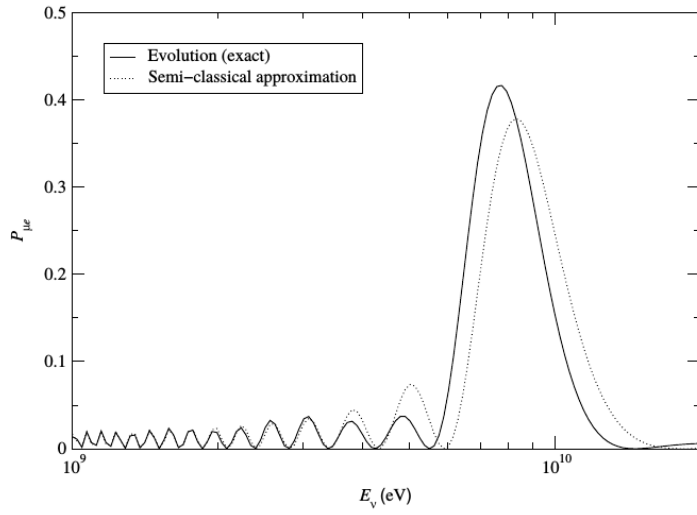


Figure A.4: Figure 1 taken from reference [16].

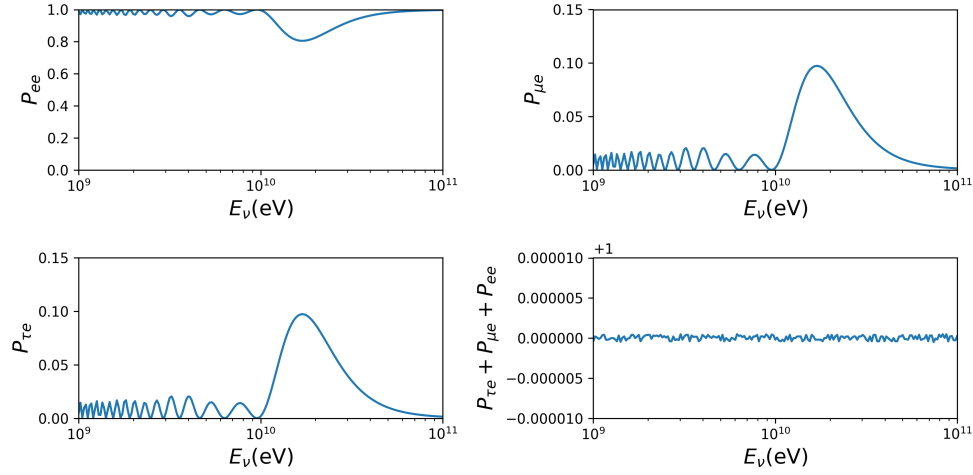


Figure A.5: UANdINO's result for figure one in reference [16].

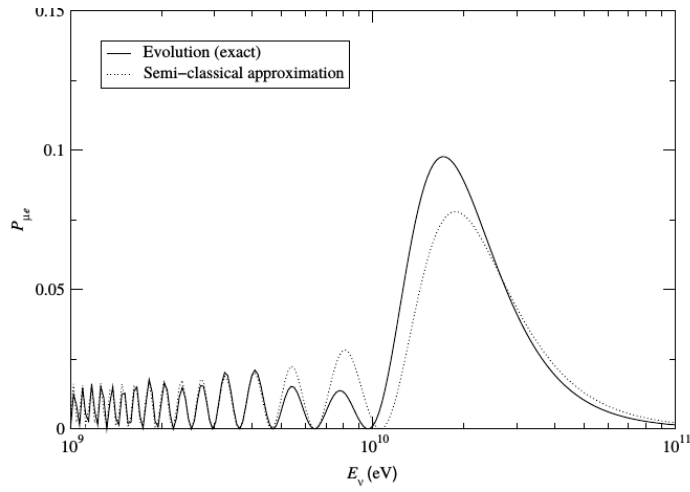


Figure A.6: Figure 3 taken from reference [16].

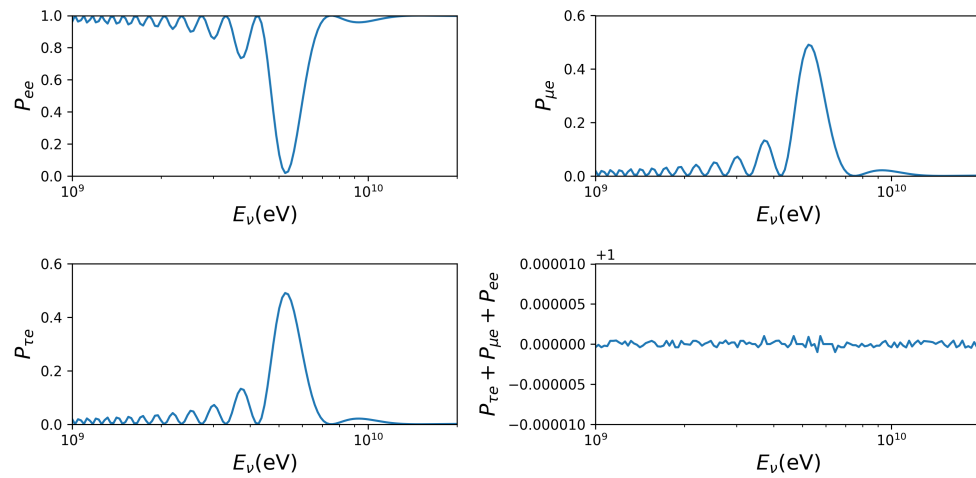


Figure A.7: UANdINO's result for figure one in reference [16].

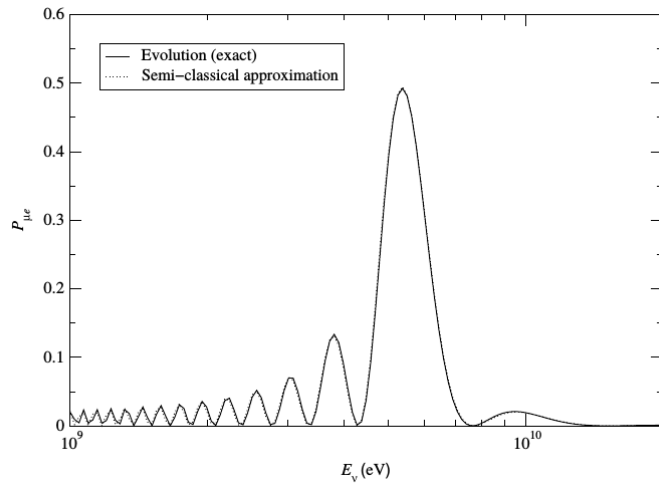


Figure A.8: Figure 4 taken from reference [16].

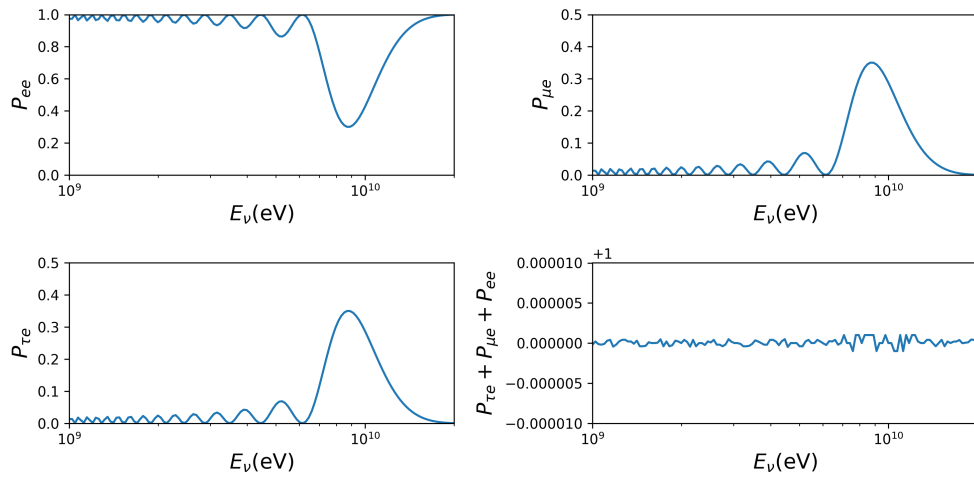


Figure A.9: UANdINO's result for figure one in reference [16].

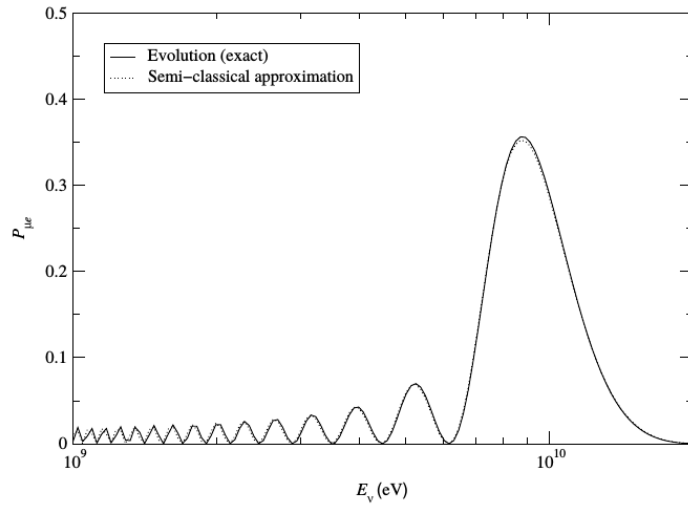


Figure A.10: Figure 5 taken from reference [16].

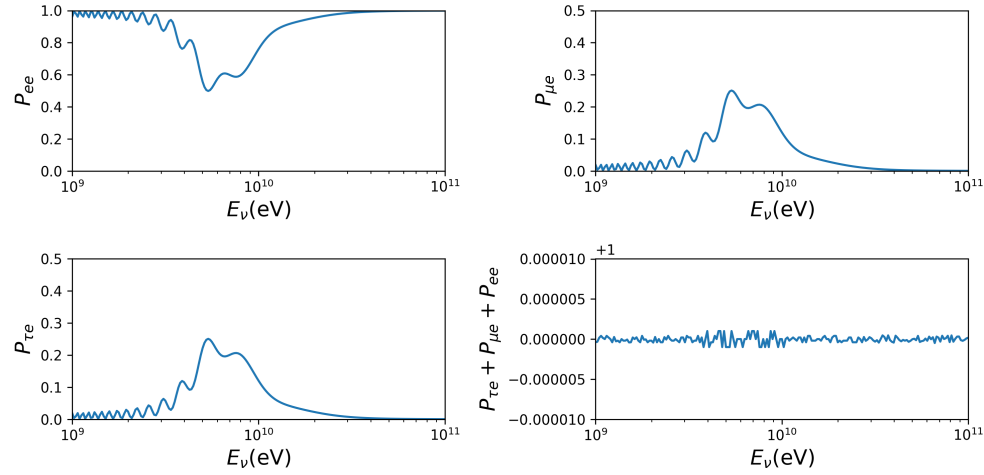


Figure A.11: UANDINO's result for figure one in reference [16].

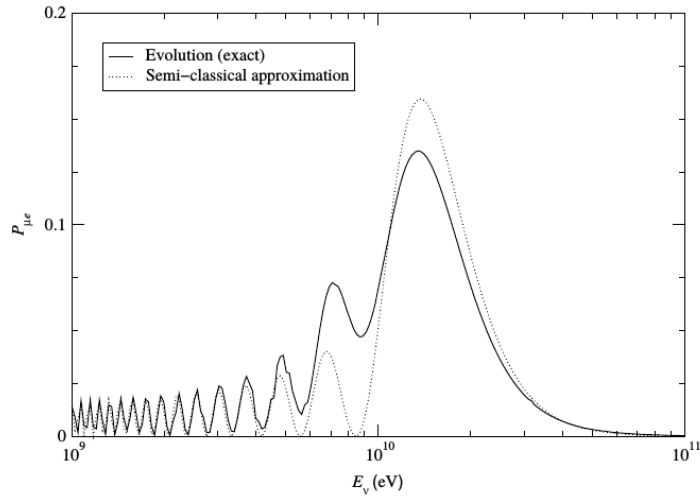


Figure A.12: Figure 6 taken from reference [16].

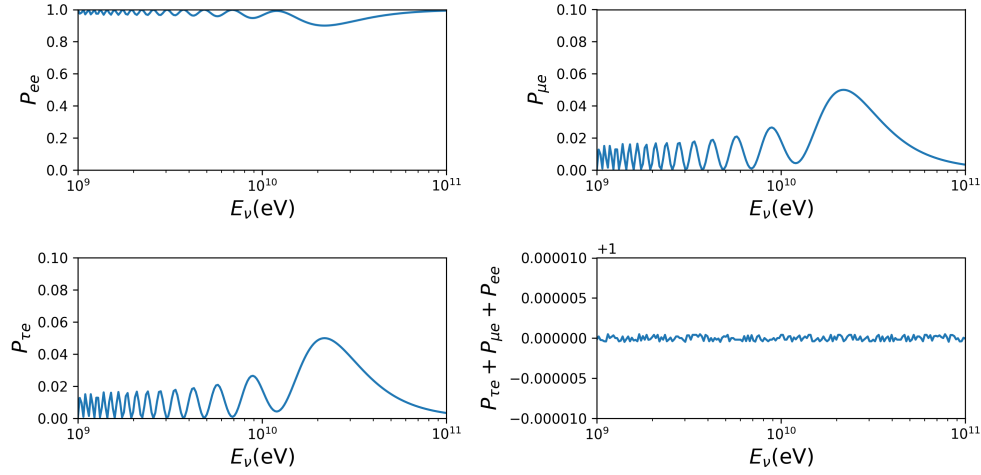


Figure A.13: UAndINO's result for figure one in reference [16].

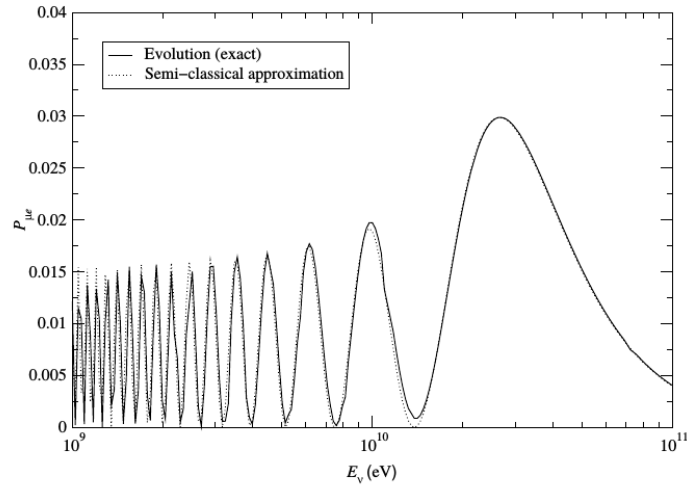


Figure A.14: Figure 7 taken from reference [16].

Appendix B

Dependence of P_{ee} on the path

Figure 8.1a shows the survival probability for the path in figure 8.1b. The following are such plots, for different paths, all of them inside the Earth. They are labeled with a pair (i, j) corresponding to a coordinate in the matrix shown in figure 6.2c.

One would expect from equation 5.37 that when L decreases, the oscillation frequency of P_{ee} will also decrease. This is well shown in figures B.1 to B.3.

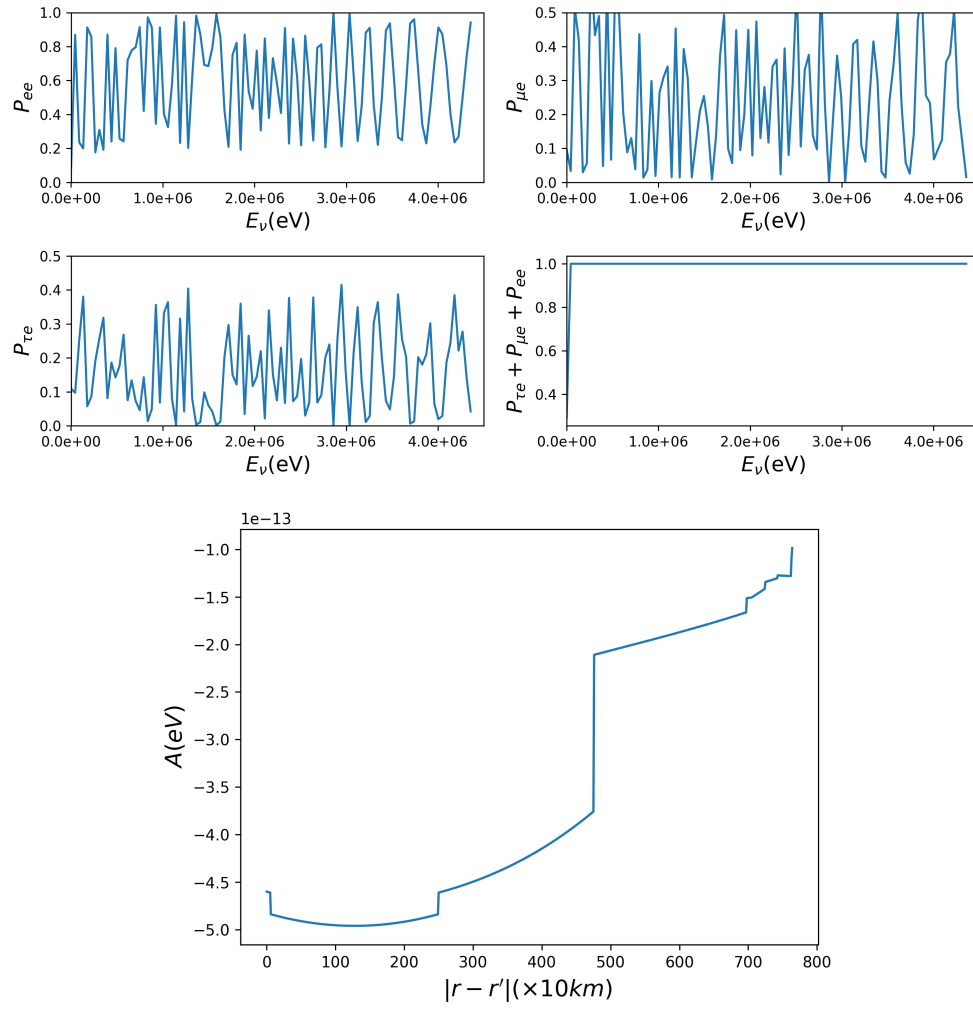


Figure B.1: Top: Survival probability of an antineutrino traveling from coordinate (1, 400) to the detector. Bottom: Potential for the path.

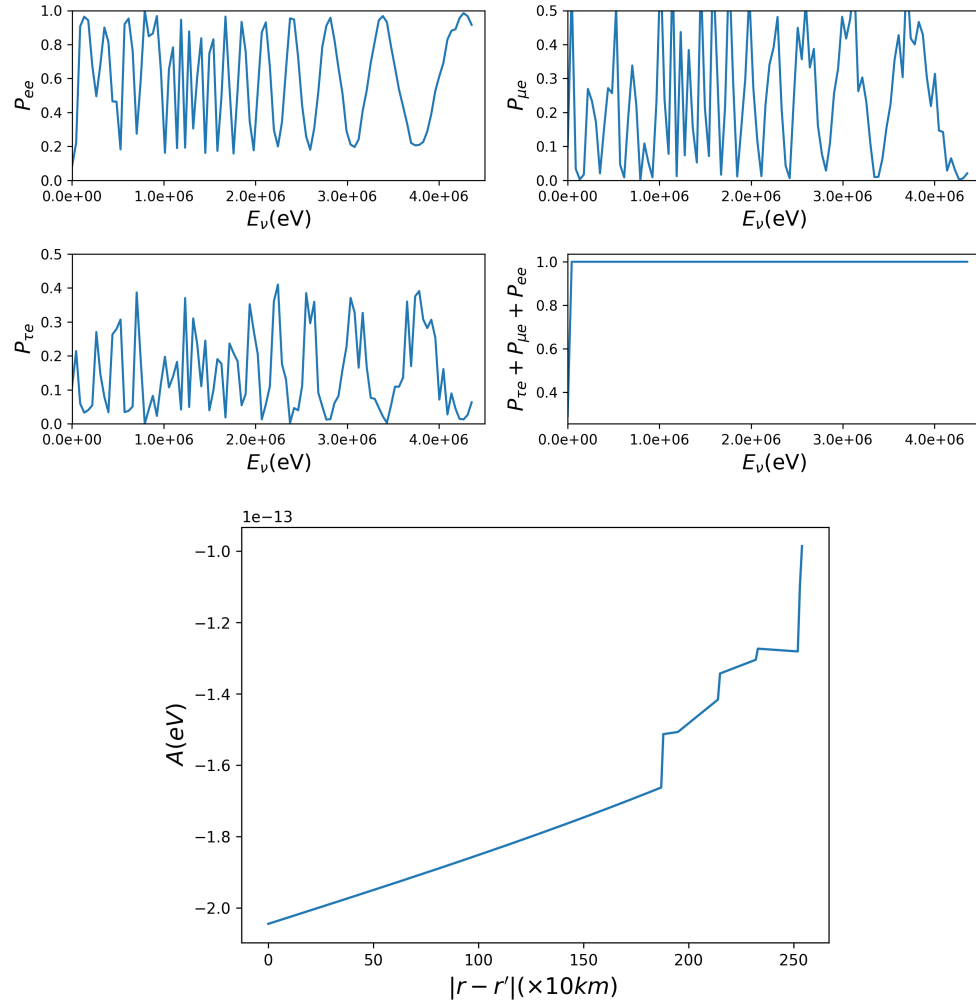


Figure B.2: Top: Survival probability of an antineutrino traveling from coordinate (1, 800) to the detector. Bottom: Potential for the path.

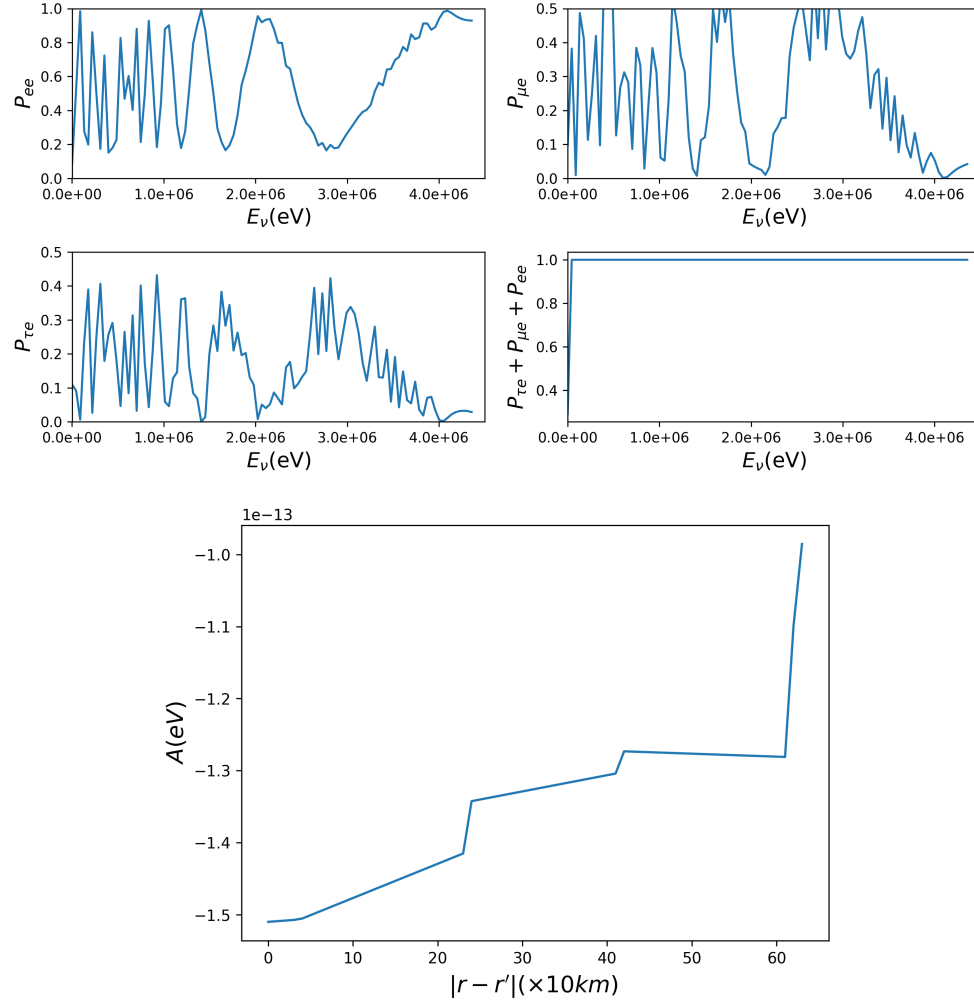


Figure B.3: Top: Survival probability of an antineutrino traveling from coordinate (1, 950) to the detector. Bottom: Potential for the path.

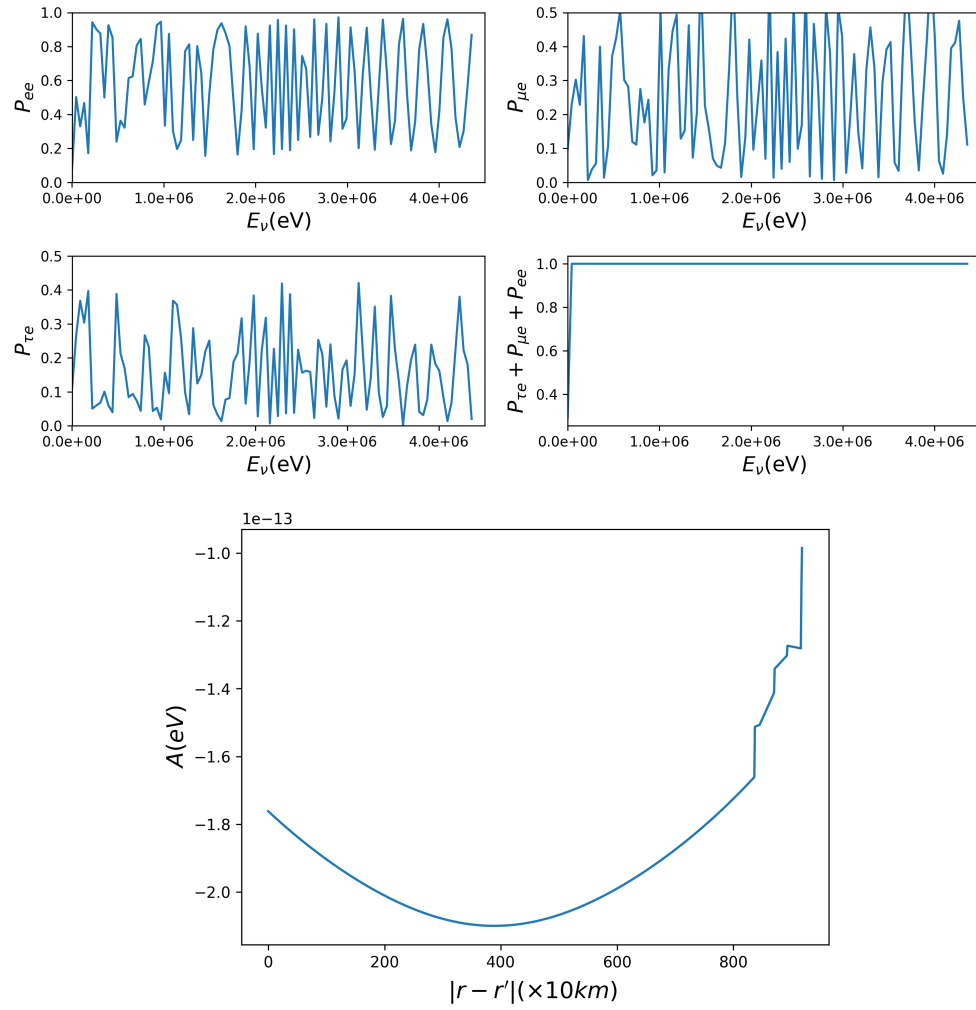


Figure B.4: Top: Survival probability of an antineutrino traveling from coordinate (400, 400) to the detector. Bottom: Potential for the path.